

8-2019

## **An Experimental Study of Thrust Augmentation with Asymmetrical Nozzle Driven Pulsed Ejector**

Orlando Rodriguez  
*The University of Texas Rio Grande Valley*

Follow this and additional works at: <https://scholarworks.utrgv.edu/etd>



Part of the [Mechanical Engineering Commons](#)

---

### **Recommended Citation**

Rodriguez, Orlando, "An Experimental Study of Thrust Augmentation with Asymmetrical Nozzle Driven Pulsed Ejector" (2019). *Theses and Dissertations*. 586.  
<https://scholarworks.utrgv.edu/etd/586>

This Thesis is brought to you for free and open access by ScholarWorks @ UTRGV. It has been accepted for inclusion in Theses and Dissertations by an authorized administrator of ScholarWorks @ UTRGV. For more information, please contact [justin.white@utrgv.edu](mailto:justin.white@utrgv.edu), [william.flores01@utrgv.edu](mailto:william.flores01@utrgv.edu).

AN EXPERIMENTAL STUDY OF THRUST AUGMENTATION WITH ASYMMETRICAL  
NOZZLE DRIVEN PULSED EJECTOR

A Thesis

by

ORLANDO RODRIGUEZ

Submitted to the Graduate College of  
The University of Texas Rio Grande Valley  
In partial fulfillment of the requirements for the degree of

MASTER OF SCIENCE IN ENGINEERING

August 2019

Major Subject: Mechanical Engineering



AN EXPERIMENTAL STUDY OF THRUST AUGMENTATION WITH  
ASYMMETRICAL NOZZLE DRIVEN PULSED EJECTOR

A Thesis  
by  
ORLANDO RODRIGUEZ

COMMITTEE MEMBERS

Dr. Isaac Choutapalli  
Chair of Committee

Dr. Robert Freeman  
Committee Member

Dr. Horacio Vasquez  
Committee Member

Dr. Robert Jones  
Committee Member

Dr. Stephen Crown  
Committee Member

Mr. Greg Acosta  
Committee Member

August 2019



Copyright 2019 Orlando Rodriguez  
All Rights Reserved



## ABSTRACT

Rodriguez, Orlando, AN EXPERIMENTAL STUDY OF THRUST AUGMENTATION WITH ASYMMETRICAL NOZZLE DRIVEN PULSED EJECTOR. Master of Science in Engineering (MSE), August, 2019, 88 pp., 81 figures, 20 references, 54 titles.

With the emergence of V/STOL vehicles and unmanned aircrafts has come the resurgence of thrust augmentation through an ejector. The use of an ejector has many benefits such as being lightweight and simple design to manufacture. In this study a hot steady jet and a cold steady/unsteady jet was tested. The hot steady jet was produced by a JetCAT PX-180 rxi with a two-inch diameter nozzle exit. The hot steady jet was compared to the cold free steady and unsteady cases. The cold jet was tested under free steady and unsteady condition, as well as steady and unsteady ejector conditions. The unsteady cold jet was produced by pulsing compressed air with a flow chopper. A direct measurement system was used to measure thrust values with and without the ejector. Four asymmetric nozzles of circular, diamond, elliptic, and rectangular were used during experimentation. Findings included that the circular, diamond, ellipse, and rectangular nozzle all performed better when under a pulsed ejector case in comparison to a steady ejector case due to the vortex ring entraining addition secondary air. It was also found that as Mach number increases thrust decreases because with higher speeds the vortex ring is no longer as organized and therefore no longer entrains as much air.





## DEDICATION

This study is dedicated to all those that came before me. To my parents who fostered my goals at every step with love and support. To the generations before them that allowed me to have the opportunities I have today. Thank you.

This study is also dedicated to my daughter Olivia Rose and her mother Milly, for always uplifting me from the rigors of being a father in graduate school. Thank you.



## ACKNOWLEDGMENT

Special acknowledgment goes to Dr. Isaac Choutapalli for chairing this study, allowing me to work as his researcher and for his in-class life lessons.

Acknowledgment also goes to the faculty and staff at the University of Texas - Rio Grande Valley, colleges, lab mates, and friends whom all played an important part in my education.



## TABLE OF CONTENTS

	Page
ABSTRACT.....	iii
DEDICATION.....	iv
ACKNOWLEDGMENT.....	v
TABLE OF CONTENTS.....	vi
LIST OF FIGURES .....	x
CHAPTER I. INTRODUCTION .....	1
Motivation.....	1
Need for Improving Thrust.....	1
Advantages of an Ejector.....	3
Background .....	5
Steady Jets .....	5
Pulsed jets .....	8
Hot and Cold Flows.....	9
Literature Review .....	10
Ejector Early Works .....	10

Entrainment of Secondary flow and its Relation to Diffusers .....	11
Similarity Solutions for Hot and Cold Flows .....	12
Ejector Geometrical Considerations .....	16
Ejector Performance Capabilities .....	19
Nozzle Geometries .....	21
Unsteady Thrust Generation .....	22
<b>CHAPTER II. EXPERIMENTAL SETUP .....</b>	<b>24</b>
Overview .....	24
Jet Turbine Test Stand .....	24
Jet Turbine .....	25
Pressure Measurements .....	27
Force Measurements .....	30
Temperature Measurements .....	32
Wiring/Connections .....	33
Data Acquisition .....	35
Pulse Jet Ejector Thrust Augmenter .....	36
Instrumentation .....	38
Air Supply .....	39
Flow Chopper .....	40

Direct Thrust Measurement System .....	41
PETA Ejector.....	42
Asymmetric Nozzles.....	43
Wiring\Connections.....	44
Data Acquisition .....	45
Load Cell Calibration .....	46
CHAPTER III. STEADY HOT JET.....	47
Overview .....	47
Jet Turbine Characterization .....	48
CHAPTER IV. PULSED COLD JET.....	54
Overview .....	54
Free Jet Thrust at Different Mach Numbers and Frequencies .....	54
Hot Steady Jet vs. Cold Steady and Unsteady Jet.....	57
Uncertainty Analysis .....	60
JTTS load Cell Uncertainty .....	61
CHAPTER V. PULSED JET EJECTOR.....	63
Overview .....	63
AR 7.6 Unsteady Thrust for Different Mach Numbers and Frequencies.....	63
AR 11 Unsteady Thrust for Different Mach Numbers and Frequencies.....	66



AR 12 Unsteady Thrust for Different Mach Numbers and Frequencies.....	68
Mach 0.1 Pulse Jet Ejector at AR 7.6, 11 and 12.....	70
Mach 0.2 Pulse Jet Ejector at AR 7.6, 11 and 12.....	74
Mach 0.3 Pulse Jet Ejector at AR 7.6, 11 and 12.....	77
1-D Theoretical Analysis for steady jet ejector.....	80
CHAPTER VI. CONCLUSIONS AND FUTURE WORK.....	84
Conclusions .....	84
Future Work .....	85
REFERENCES .....	86
BIOGRAPHICAL SKETCH .....	88

## LIST OF FIGURES

	Page
Figure 1: F-35B vertical landing taken from Lockheed Martin picture archives .....	2
Figure 2: Schematic of nozzle/ejector relationship and jet and ambient flow movement into ejector .....	4
Figure 3: Basic design of a turbojet engine .....	6
Figure 4: Pratt & Whitney GP7200 Turbofan taken from Pratt & Whitney archives .....	7
Figure 5: PIV of vortex rings taken from (Choutapalli I. M., An Experimental Study of a Pulsed Jet Ejector, 2007) .....	8
Figure 6: Relationship between primary to secondary flow areas at inlet, diffuser area ratio and mass flow rate ratio from (Heiser W. , 2010) .....	11
Figure 7: Stagnation pressure and Mach number changes due to mixing from (Presz & Greitzer, 1988).....	14
Figure 8: Compressible pumping from (Presz & Greitzer, 1988) .....	15
Figure 9: thrust augmentation results from several references from (Presz & Greitzer, 1988).....	15
Figure 10: Straight (SE) and diverging (DE) PDE-ejector thrust augmentation variation with fill fraction for three ejector L/D ratios from (Allgood, Ephraim, Hoke, & Bradley, 2008) .....	17

Figure 11: Ejector schematic including streamlines of primary and secondary streams and their subsequent mixing inside the ejector from (Presz, Reynolds, & Hunter, 2002).....	18
Figure 12: Thrust augmentation as a function of ejector inlet rounding for various ejector diameters and lengths with fixed distance between ejector inlet and nozzle exit from (Paxson, Wilson, & Dougherty, 2002) .....	19
Figure 13: Thrust augmentation of an ideal ejector according to momentum theory from (Bevilaqua, 1987) .....	20
Figure 14: Effect of losses on ejector thrust augmentation from (Bevilaqua, 1987) .....	20
Figure 15: Axis switching of elliptic, square, rectangular, equilateral triangle and isosceles triangle from (Miller, Madnia, & P., 1996).....	21
Figure 16: Jet Turbine Test Stand (JTTS).....	25
Figure 17: JetCAT P180-RXi internal view .....	26
Figure 18: Omega PX313 series pressure transducer .....	27
Figure 19: PX313 calibration on PCL819 device .....	28
Figure 20: Front plate pressure transducer mount .....	28
Figure 21: Schematic of pitot probe.....	29
Figure 22: Pitot traversing mechanism .....	30
Figure 23: LC302-50 schematic.....	31
Figure 24: Thrust measurement technique.....	31
Figure 25: Load cell calibration technique .....	32
Figure 26: Inlet and exit thermocouple placement .....	33
Figure 27: Block diagram of JTTS system .....	33

Figure 28: Fuel System .....	34
Figure 29: Graphic user interface of LabVIEW code .....	36
Figure 30: Schematic of Pulse Jet Ejector Augmenter from Choutapalli, 2007 .....	37
Figure 31: Chamber thermocouple, pressure transducer and nozzle pressure transducer placement.....	39
Figure 32: load cell placement within thrust balance .....	39
Figure 33: Pressure valve system.....	40
Figure 34: Schematic representation of flow chopper .....	41
Figure 35: Direct thrust measurement system .....	42
Figure 36: Schematic representation of PETA ejector .....	43
Figure 37: Asymmetric nozzles from left to right; circular, diamond, ellipse and rectangular .....	43
Figure 38: Block Diagram of PETA system.....	44
Figure 39: Digital displays collected on a single panel .....	45
Figure 40:Thrust balance calibration method which includes a pulley system used to measure known loads. ....	46
Figure 41: Jet turbine directional establishment .....	47
Figure 42: Exit gas temperature as a result of increasing RPM at nozzle exit .....	48
Figure 43: Pressure at exit of nozzle as a result of increasing RPM.....	48
Figure 44:Pressure taken at 33,80 and 120 RPM with increasing axial distance .....	49
Figure 45: Stagnation pressure taken at 33RPM with increasing lateral distance at different axial distances.....	50

Figure 46: Stagnation pressure taken at 80RPM with increasing lateral distance at different axial distances.....	51
Figure 47: Stagnation pressure taken at 120RPM with increasing lateral distance at different axial distances.....	51
Figure 48: Jet turbine Mach number as a result of increasing RPM.....	52
Figure 49: Jet turbine thrust as a function of Mach #.....	53
Figure 50: Mach 0.1; thrust against frequency comparing circle, diamond, ellipse and rectangle nozzle geometries for a free jet.....	54
Figure 51: Mach 0.2; thrust against frequency comparing circle, diamond, ellipse and rectangle nozzle geometries for a free jet.....	55
Figure 52: Mach 0.3; thrust against frequency comparing circle, diamond, ellipse and rectangle nozzle geometries for a free jet.....	55
Figure 53: thrust vs Mach # for PETA nozzle shapes at steady conditions and JTTS standard circle nozzle at steady conditions .....	57
Figure 54; thrust vs Mach # for PETA nozzle shapes at 30Hz and JTTS standard circle nozzle at steady conditions.....	58
Figure 55: thrust vs Mach # for PETA nozzle shapes at 60Hz and JTTS standard circle nozzle at steady conditions.....	58
Figure 56: thrust vs Mach # for PETA nozzle shapes at 90Hz and JTTS standard circle nozzle at steady conditions.....	59
Figure 57: Mach 0.1; thrust against frequency comparing circle, diamond, ellipse and rectangle nozzle geometries for a jet ejector AR 7. ....	63

Figure 58: Mach 0.2; thrust against frequency comparing circle, diamond, ellipse and rectangle nozzle geometries for a jet ejector AR 7.6 .....	64
Figure 59: Mach 0.3; thrust against frequency comparing circle, diamond, ellipse and rectangle nozzle geometries for a jet ejector AR 7.6 .....	64
Figure 60: Mach 0.1; thrust against frequency comparing circle, diamond, ellipse and rectangle nozzle geometries for a jet ejector AR 11 .....	66
Figure 61: Mach 0.2; thrust against frequency comparing circle, diamond, ellipse and rectangle nozzle geometries for a jet ejector AR 11 .....	66
Figure 62: Mach 0.3; thrust against frequency comparing circle, diamond, ellipse and rectangle nozzle geometries for a jet ejector AR 11 .....	67
Figure 63: Mach 0.1; thrust against frequency comparing circle, diamond, ellipse and rectangle nozzle geometries for a jet ejector AR 12 .....	68
Figure 64: Mach 0.2; thrust against frequency comparing circle, diamond, ellipse and rectangle nozzle geometries for a jet ejector AR 12 .....	69
Figure 65: Mach 0.3; thrust against frequency comparing circle, diamond, ellipse and rectangle nozzle geometries for a jet ejector AR 12 .....	69
Figure 66: Mach 0.1; Circle nozzle with an ejector; thrust against AR at steady and unsteady cases .....	70
Figure 67: Mach 0.1; Diamond nozzle with an ejector; thrust against AR at steady and unsteady cases .....	71
Figure 68: Mach 0.1; Elliptic nozzle with an ejector; thrust against AR at steady and unsteady cases .....	71

Figure 69: Mach 0.1; Rectangle nozzle with an ejector; thrust against AR at steady and unsteady cases .....	72
Figure 70: Mach 0.2; Circle nozzle with an ejector; thrust against AR at steady and unsteady cases .....	74
Figure 71: Mach 0.2; Diamond nozzle with an ejector; thrust against AR at steady and unsteady cases .....	75
Figure 72: Mach 0.2; Elliptic nozzle with an ejector; thrust against AR at steady and unsteady cases .....	75
Figure 73: Mach 0.2; Rectangle nozzle with an ejector; thrust against AR at steady and unsteady cases .....	76
Figure 74: Mach 0.3; Circle nozzle with an ejector; thrust against AR at steady and unsteady cases .....	77
Figure 75; Mach 0.3; Diamond nozzle with an ejector; thrust against AR at steady and unsteady cases .....	78
Figure 76: Mach 0.3; Elliptic nozzle with an ejector; thrust against AR at steady and unsteady cases .....	78
Figure 77: Mach 0.3; Rectangle nozzle with an ejector; thrust against AR at steady and unsteady cases .....	79
Figure 78: Ejector schematic establishing C.V.....	81
Figure 79: Ejector pumping as a function of area ratio .....	83
Figure 80: Exploded view of ejector prototype .....	85
Figure 81: Ejector prototype CAD model.....	85

## CHAPTER I

### INTRODUCTION

#### **Motivation**

The motivation for this study comes from the reemergence of ejector technology for its promising applications towards V/STOL and unmanned aircraft. Ejectors have the ability to improve thrust while having the advantage of being a simple, lightweight mechanism. This is further expressed in the following sections.

#### **Need for Improving Thrust**

Improvements in thrust performance is an ongoing need as an increase in thrust would mean optimal takeoff, more efficient travel and subsequent lower costs to operate for aeronautic vehicles. This is especially true for aeronautic vertical or short take-off and landing (V/STOL) aircraft in the battlefield and for unmanned aircraft. During combat, aircraft must have the ability to react quickly and become airborne as rapidly as possible. This is not always the case especially for fighter jets onboard of an aircraft carrier. Fighter jets are sent off one by one through the aircraft carriers' single runway, causing extended time for mission takeoffs and is less than ideal for the military. The solution to this seems to apply a V/STOL system onto the fighter jets itself. The idea comes from helicopters having the ability to takeoff faster than a jet fighter because there is no need for a runway. Lockheed Martin's F-35B jet fighter is the world's first fighter short



takeoff/vertical landing vehicle (STOVL). The F-35B has an engineered jet turbine which can point downwards during takeoff to promote a shorter takeoff. The F-35B also has another engine near the center of the aircraft called the lift fan which in conjunction with the turbine in back allows for a vertical landing. This makes the F-35B the most efficient aircraft to allow multi-takeoff and



*Figure 1: F-35B vertical landing taken from Lockheed Martin picture archives*

landing onboard an aircraft carrier or a landing strip and gives a glimpse at the power of VSTOL and STOVL.

Thrust performance increases can also benefit commercial airlines. Air travel is the most efficient means of mass travel in the United States with about 87,000 flights taking the air every day. Airlines spend around 40% of their operating cost on fuel consumption alone. Much of the fuel consumption on short to mid-range flights happens on take-off and the climb to cruise altitudes. This is because of the increased drag effects at atmospheric levels due to higher pressures compared to the thinner air at cruising conditions. With an increase to thrust performance, cost of fuel would be reduced and the subsequent cost for a plane ticket would also theoretically drop.

With higher thrust capabilities also comes the added advantage of being more environmentally friendly. According to a 2010 NASA report, 25% of emission for short and mid-range flight came from taxiing and takeoff. This correlates to the majority of fuel consumption happening at take-off and climbing because of the difficulty to fly against drag to produce enough lift to reach cruise conditions. If commercial aircraft saw an increase in thrust capabilities the consequent carbon footprint would also be reduced.

### **Advantages of an Ejector**

Though the F-35B has the ability to have a short takeoff and vertical landing, the optimum goal is to have both rapid vertical takeoff and vertical landing. As is now the propulsion system onboard the F-35B does not produce enough thrust and is incapable of a pure and rapid vertical takeoff. Installing larger turbines could produce enough thrust but would be less ideal when considering the total weight of the aircraft. A potential solution comes in the form of technology called an ejector. An ejector is an addition piece of technology which is placed aft of a jet stream and requires no additional moving part. The ejector is relatively lightweight and depending on construction can be relatively short. In this study an ejector will be used in combination with a convergent nozzle to increase the thrust output of a jet. A schematic of the relationship between the nozzle and the ejector can be seen in Figure 2. The ejector is a shroud which surrounds the exit gas coming from the turbojet nozzle as can be seen from the red arrow in Figure 2. When the exit gas passes through the ejector, outside ambient air is also entrained into the ejector as can be seen by the blue arrows in Figure 2. The ambient air mixes with the exhaust gas through shear mixing and an increased mass flow rate is created and pushed out of the ejector creating higher thrust. The

mixing of the two streams is of great importance for a higher thrust output and is an aim for this study.

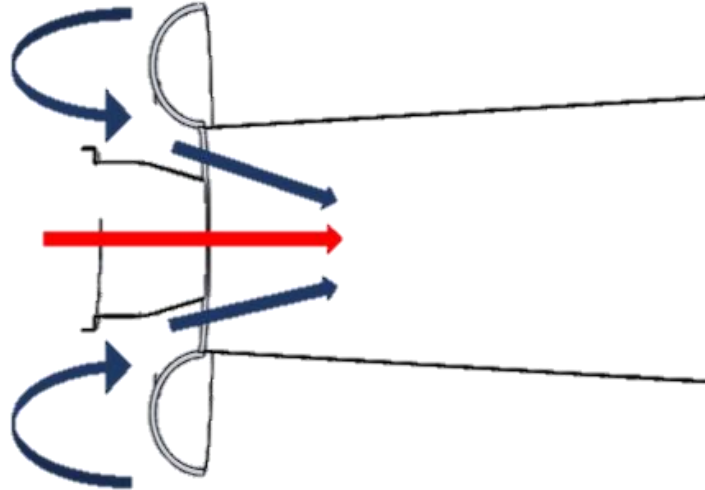


*Figure 2: Schematic of nozzle/ejector relationship and jet and ambient flow movement into ejector*

An important way of determining the efficiency of an ejector is by calculating the thrust augmentation ratio ( $\Phi$ ) which is defined as the total thrust compared to a reference thrust. In the case of this research the total thrust will be the thrust produced by a combination of a nozzle and an ejector. The reference thrust will be the thrust produced by the nozzle alone. The thrust augmentation will be a center point in determining the improvement of performance by the ejector and will be derived later in the report.

$$\Phi = \frac{\text{Total Thrust}}{\text{Reference Thrust}} \quad (1.1)$$

To improve thrust augmentation different design parameters can be implemented such as ejector inlet shape, diverging or straight shroud, length of the shroud itself and the area ratio (AR), which is the fraction of ejector inlet area over the area of the turbine nozzle in this case. These different design parameters will be explained throughout the report.

## **Background**

For this study, it is important to distinguish the difference between steady and pulsed jets as well as hot and cold flows. The following further investigates the differences.

### **Steady Jets**

The widely used propulsion engines; turbojets, turbofans and rockets are all considered to be steady jets. A turbojet engine is an air breathing fuel injected device comprised of rotating fans (Figure 3). The turbojet engine begins by sucking in air at the front of the device with a fan. The compressor made up of many smaller fans which can range from one row to many rows rotates at high speeds and compresses the air and raises the pressure. The compressed air is then passed to a combustion chamber where fuel is added, and a spark ignites the air/fuel combination. The burning air/fuel combination becomes a hot gas and rapidly expands through nozzle and out of the turbojet. This in turn creates the thrust propelling the turbojet forward. As the hot exhaust gasses exits the nozzle it first passes the turbine. The turbine is connected to the same shaft as compressor and works as sort of the motor of the compressor to keep the system running continuously.

A turbofan has all the same components as a turbojet engine with the added components of a large fan in the front and additional turbine in the back. These two added components are concentrically connected over the existing shafts. The added fan sends some of the air around the core of the turbine and creates a bypass which is eventually joined at the exhaust. This creates more thrust for the turbofan and acts as noise suppressor for the aircraft.

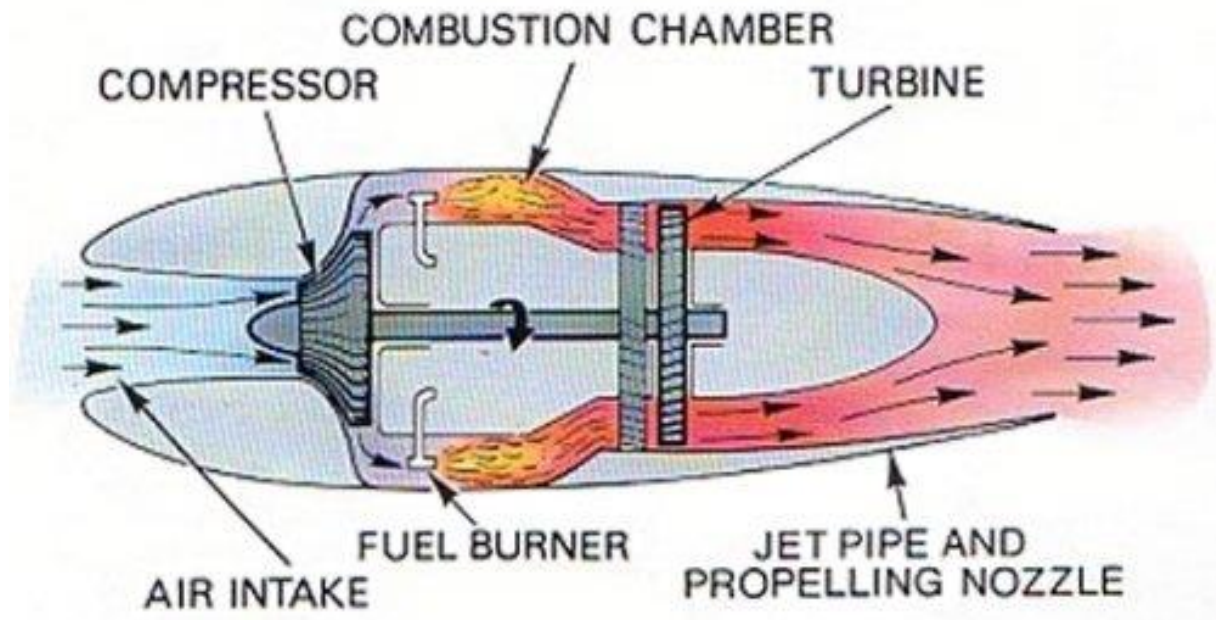


*Figure 3: Basic design of a turbojet engine*

Rocket engines are another propellant engine but differ from turbojets and turbofans in that they do not use air from the atmosphere as the working fluid. Rocket engines use fuel and a source of oxygen and are mixed in a combustion chamber. The fuel/air mixture is highly compressed and highly heated which is sent to the rocket's nozzle where the thrust is subsequently produced. There are many types of rocket engines, but the two main categories are solid rockets and liquid rockets. Liquid rockets store the fuel and oxidizer in separate containers before being introduced to the combustion chamber, while solid rockets the fuel and oxidizer are mixed and packed together in a single container.

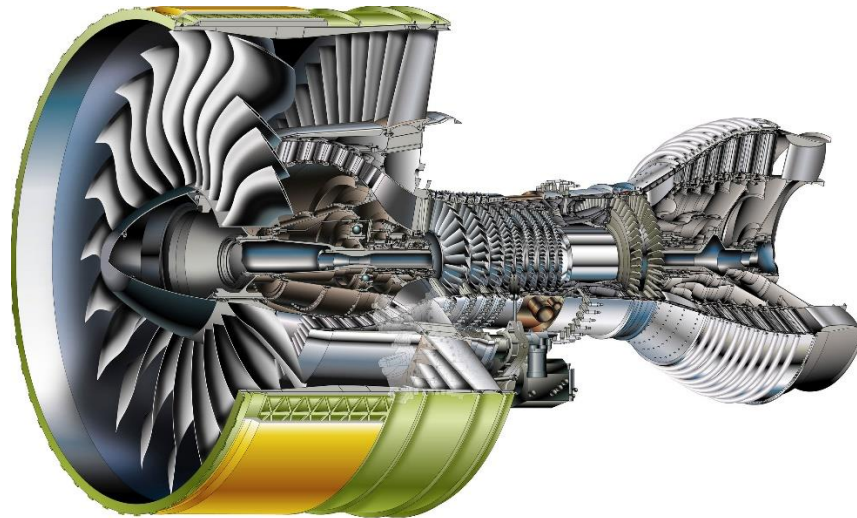


*Figure 4: Pratt & Whitney GP7200 Turbofan taken from Pratt & Whitney archives*

Like much technology, there are limitations to the performance and thrust a turbojet can produce. A turbojet engine's performance is highly dependent on the temperatures and pressures the engine can produce internally. With this comes the difficulty in designing an engine that can withstand extreme temperatures. The material of the compressor, combustion chamber, turbine, nozzle, and overall case must be meticulously engineered in order to maintain the intense temperatures and pressures as well as be light enough as to not become too much of a weight burden on the overall aircraft. This entails extensive research on alloyed metal, composites, and their subsequent material properties. The above-mentioned propulsion engines also perform differently at different altitudes along their flight paths. As the vehicle takes off, aeronautic vehicles require the most thrust output from the propulsion engines to overcome the effects of gravity. During climb to reach cruising altitude the vehicle also requires high thrust output due to the effects of drag from the relatively thick air closer to the ground. Once the vehicle reaches cruising altitude the propulsion engine no longer works as hard due to the reduced effects of gravity

and runs more efficiently. Due to propulsion engines needing to have the greatest thrust output in during takeoff, much research such as this takes aim at improving VSTOL and STOVL aeronautic vehicles.

## Pulsed jets

A pulsed jet is formed by disturbing the flow of a steady jet which creates intermitted pulses. The way in which the disturbances are created has been done though varies methods throughout the years. Early methods of pulsing were done using a piston driver or through a valves shock tube. Some other familiar method of pulsing was created using rotating valves, reciprocating engines, pulse detonation engines (PDE), and in this study by a rotating disk. An obscure method of creating pulses includes the use of load speakers to disturb the flow. The disturbances are usually continuously repeated and can be described by the frequency in which the pulses are created. Pulsed jets are known to produce more thrust than their steady jet counter parts.

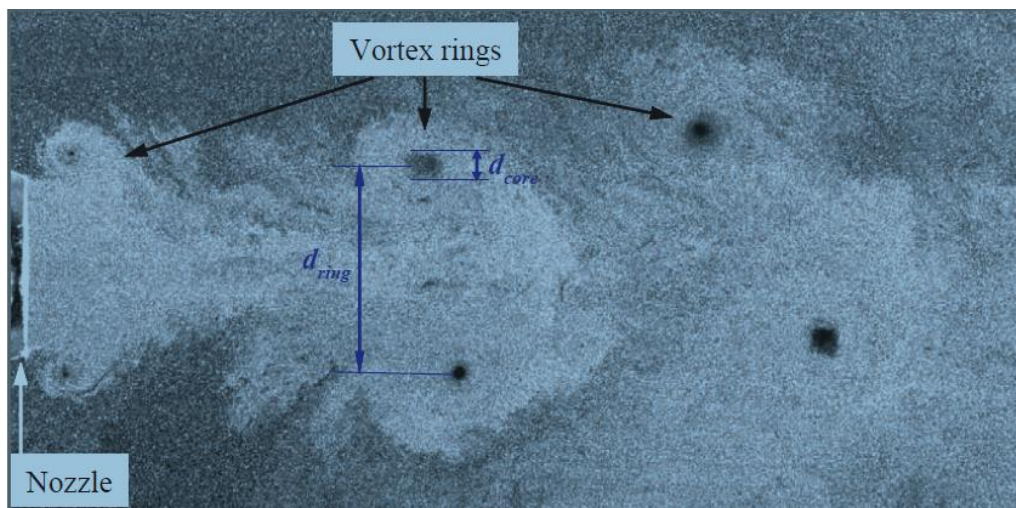


Figure 5: PIV of vortex rings taken from (Choutapalli I. M., An Experimental Study of a Pulsed Jet Ejector, 2007)

The increase in thrust can be traced to the formation of vortex rings. As explain in (Choutapalli I. M., An Experimental Study of a Pulsed Jet Ejector, 2007) a vortex ring is created

by the vorticity layer rolling up as a pulse is generated from the flow expanded out of a nozzle. This rolled up layer is met with ambient air which is entrained into the vortex and further accelerates and enlarges the vortex ring. The vortex ring along with the addition entrainment of ambient air produces the addition thrust that is greater than its steady counterpart. Though the pulse jets produce more thrust they are not widely used in aeronautic vehicles. This is because they are difficult to install when scaled up onto aircrafts due to their substantial vibration and noise from the pulses. When scaled down, pulse jets have made improvements on smaller aircraft such as unmanned drones.

### **Hot and Cold Flows**

Two types of jet flows will be studied in the paper for the purpose of comparison and potential crossover in design application. A cold flow pulse jet which is described in (Choutapalli I. M., An Experimental Study of a Pulsed Jet Ejector, 2007) will be further advanced in experimentation through the addition of various axisymmetric nozzle configurations. A steady hot flow is also studied, in which a jet turbine is studied. The purpose of presenting both jet types is to compare the results of the cold flow to the potential results of the hot flow. Cold flow jets present the ability to readily test as compared to hot flow jets. With this we can utilize the results from the cold jet and its configuration that lead to those results with the hopeful future application to the hot jet. The ultimate outcome of this study and future studies is to apply all configuration and setup learned from the cold jet and apply them to the hot jet. Since hot jets are what is currently used on mainstream aircraft the ability to go from cold jet to hot jet is of relative importance.



## **Literature Review**

A literature review was done for this study which investigated various topics ranging from ejector development through time, to specific design parameters that will be used for future studies.

### **Ejector Early Works**

Much of the work done with ejectors and improving the parameter of thrust augmentation has been in cold flow pulsed jet. It has been repeated time and again that greater thrust augmentation can be produced when using a pulsed jet compared to a steady jet. Some of the very first studies into thrust augmentation through an ejector was done by Lockwood (R.M., 1963). Lockwood hypothesized that an intermediate jet (pulsed jet) acts as a piston and that the exchange between primary pulsed jet and a secondary jet is an exchange between pressures. This was experimentally compared to an exchange between a free jet and a secondary jet. In the test Lockwood used an augment with a throat area of ejector to primary jet (area ratio) of 4-10 and a length to throat diameter ratio of 1-1.5. The intermittent jet produced 60-140% more thrust than the free stream jet alone. When used with the free stream jet the thrust augmentation was less than 20%. He attributed the unsteady ejector performance to a more efficient energy transfer process between the primary flow and the secondary (entrained) flow through inviscid processes, whereas the steady ejector relies primarily on viscous shear mixing. Some of the top applications for steady ejectors has come in the field of noise suppression as stated in (Presz, Reynolds, & Hunter, 2002) where the mixing of cold air into the hot exhaust provides a means of noise suppression.

## Entrainment of Secondary flow and its Relation to Diffusers

The entrainment of the secondary flow into the ejector from the primary flow is the most important process when trying to improve thrust performance through an ejector. (Heiser W. , 2010) defines this mechanism as the spread of energy resident in the primary flow to the secondary flow. Heiser goes on to conduct an ejector-diffuser mass and momentum analysis for steady flow ejectors to highlight the importance of the diffuser as part of the ejector design. Assumptions were made in the analysis such as primary and secondary flows have constant density, isentropic upstream of the ejector inlet and the walls of the ejector are frictionless. A thrust augmentation ratio was developed based on these assumptions which included variables for primary and secondary mass flow rates, densities, primary to secondary flow areas at the inlet ( $\alpha$ ) and ratio of diffuser exit area to entrance area ( $\beta$ ). The finding of the analysis were that thrust augmentation is independent of total pressure (unlike its dependence on net thrust on the isentropic primary flow), and that increasing  $\beta$  or decreasing  $\alpha$  will increase mass flow rate ratio therefor meaning the diffuser increases mass flow rate.

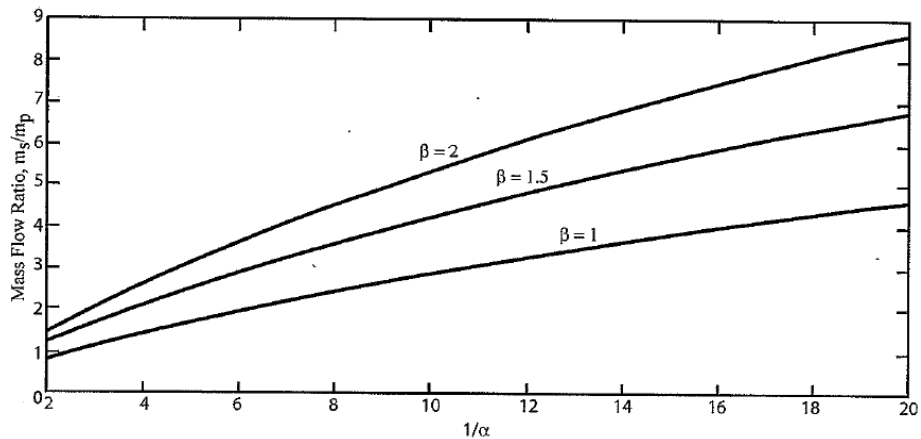


Figure 6: Relationship between primary to secondary flow areas at inlet, diffuser area ratio and mass flow rate ratio from (Heiser W. , 2010)

Heiser also goes on to point out that the static pressure exerted on the walls of the exhaust diffuser is below atmospheric which creates a drag on the diffuser. This means that the additional thrust produced by the diffuser is entirely due to the reduced static pressure exerted on the entrance of the ejector which was caused by the increased secondary flow mass flow and velocity. This becomes an important result as it tells us that the entrainment of the secondary flow must be done in such a way as to not cause flow separation which would negate the results mentioned above. A bell mouth at the entrance of the ejector is traditionally used to help the secondary flow along into the ejector. Other more advanced methods of ejector-diffuser designs include sophisticated injection methods of the primary flow called hyper mixing nozzles and diffuser boundary layer control also called end wall energization.

### **Similarity Solutions for Hot and Cold Flows**

Since the experiments in this paper will be done using both hot flow and cold flow jets it is useful to establish a correlation between hot flow and cold flow ejectors. In (Presz & Greitzer, 1988) a similarity principle in accordance with the development in (Greitzer, Paterson, & Tan, 1985) was used to prove that a range of temperature distributions does not affect thrust augmentation performance and is only a factor of geometrical considerations of an ejector. Presz uses an Approximate Munk and Prim similarity principle to determine his findings (Notice this is an approximate and not the Munk and Prim principle itself). The Munk and Prim similarity principle holds for any steady flow in which the streamlines can be determined to be isentropic and is a perfect gas with constant specific heat. The similarity principle as derived by Greitzer (Eqn. 1.2) is obtained from the continuity and momentum equations using the initial conditions mentioned previously and is written in terms of Mach number and stagnation pressure. In Eqn.

1.2, the stagnation enthalpy does not appear and therefore the Mach number and pressure fields do not change in the flow with respect to stagnation temperature distribution.

$$(M \cdot \Delta)M - \frac{\gamma-1}{\gamma+1} M(\nabla \cdot M) - \frac{1}{\gamma-1} \nabla \left\{ \ln \left[ 1 + \frac{\gamma-1}{2} M^2 \right] \right\} + \frac{1}{\gamma} \nabla \ln P_t = 0 \quad (1.2)$$

Presz goes on to extend the Munk and Prim similarity principle by investigating an injection model problem and a two-stream model problem. The injection model problem derived an incremental change in a stream flow of a constant area duct and yielded a result that stagnation pressure is compensated by increased injected velocity. This small change in stagnation pressure yields a small change in stagnation temperature which can be taken as negligible. The two-stream problem looks at mixing two streams of equal area in which a control volume analysis was done. The results were plotted and are shown here in Figure 7. The vertical axes represent the non-dimensional pressure difference (stream 1 at inlet to full mixed) and Mach number at exit mixed condition compared to inlet Mach number. The horizontal axis represents the dynamic pressure ratio. The primary to secondary temperature ratios (TR) used were 0.5, 1.0, 2.0 and 3. The top cluster of curves though changes dramatically in Mach ratio with changing dynamic pressure ratio does not deviate with changing TR. The bottom cluster which compares the pressure difference to the dynamic pressure ratio also gives similar results and shows that in mixing ducts the temperature distribution can be taken as negligible.

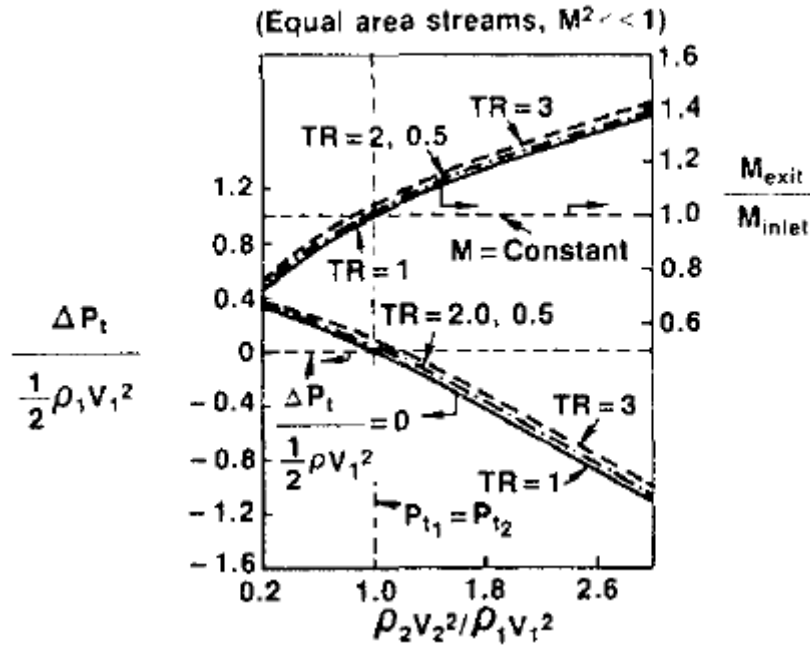


Figure 7: Stagnation pressure and Mach number changes due to mixing from (Presz & Greitzer, 1988)

Presz goes on to apply this approximation to ejector nozzles in which he focuses control volume analysis on the area in which the primary and secondary streams mix in an ejector. Eqn. 1.3 does not show a stagnation pressure difference therefore temperature can also be neglected.

$$\sqrt{\frac{Q_p}{Q_s} \left( \frac{\dot{m}_s}{\dot{m}_p} \right)} \quad \text{or} \quad \sqrt{\frac{T_{ts}}{T_{tp}} \left( \frac{\dot{m}_s}{\dot{m}_p} \right)} \quad (1.3)$$

Resulting in the following figures,

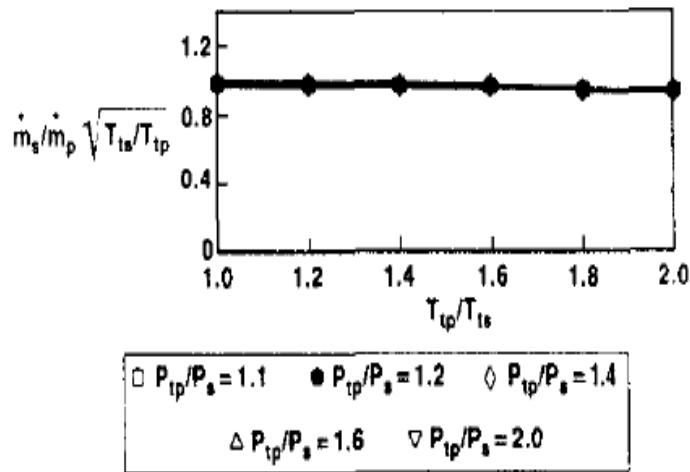


Figure 8: Compressible pumping from (Presz & Greitzer, 1988)

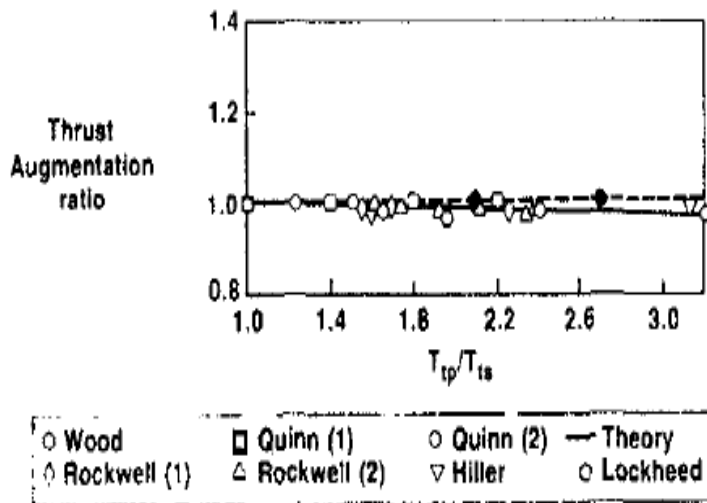


Figure 9: thrust augmentation results from several references from (Presz & Greitzer, 1988)

The above figures are the analytic model results for supersonic flows as done by Presz. Figure 8 shows the mass flow rate is unmoved by the temperature ratio. Figure 9 shows the thrust augmentation ratios from several other known works and displays the same result in which the

temperature ratio has little to no effect on thrust augmentation. The results conclude that ejectors are indifferent to temperature ratios and are largely a function of geometric considerations.

### **Ejector Geometrical Considerations**

The size and geometry of an ejector are important to its performance in increasing thrust augmentation. The thrust performance will be a factor of the amount of ambient air which can be entrained into the ejector by the primary stream. The length of the ejector along with the geometrical shape (square/circular and so on), straight or divergent sections and inlet shape must all be taken into consideration. There is unfortunately no analytical analysis to determine these parameters when designing an ejector, but instead experimental studies have been done to give a better indication on the benefits of using certain parameters.

In (Allgood, Ephraim, Hoke, & Bradley, 2008) two sets of ejectors were tested; straight cylindrical ejectors and straight cylindrical ejectors with a diverging exhaust end piece to find the effects of divergent angles. A fill-fraction, which is the percent in which the shock tube is filled with gas mixture that detonates in the pulse detonation engine (PDE) was used to standardize the experiment. Figure 10 shows the results of the experiment. The experiments determined that diverging ducts performed better than straight ducts and that higher fill fractions thrust augmentation performance went down due to effects of drag. Allgood found that the addition thrust surface area provided by the divergent angle accounted for the higher augmentation. Allgood also studied the effects of distance from the primary stream to the ejector but found that the results were highly dependent on the fill fraction and could not determine the importance of the distance.

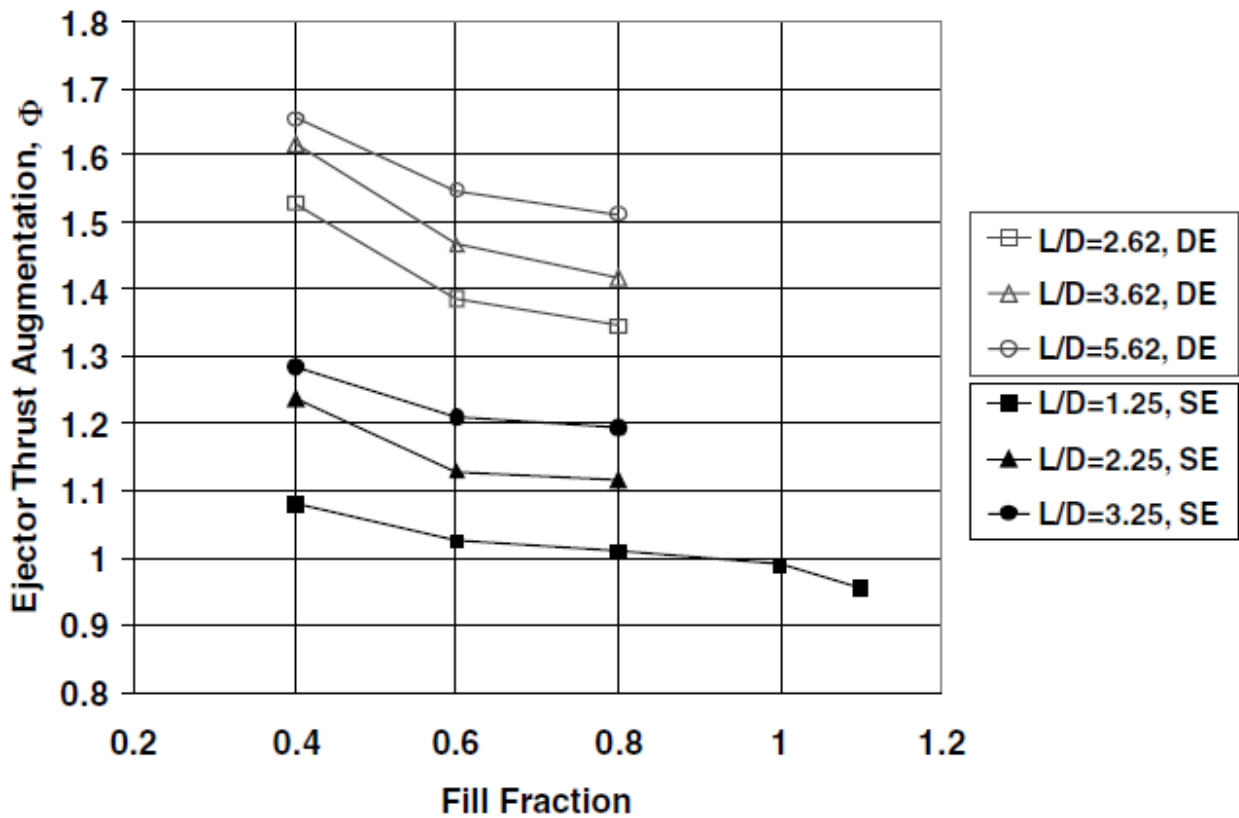


Figure 10: Straight (SE) and diverging (DE) PDE-ejector thrust augmentation variation with fill fraction for three ejector L/D ratios from (Allgood, Ephraim, Hoke, & Bradley, 2008)

An ejectors performance relies heavily on the ability of the primary flow to entrain the secondary flow in order to mix inside of the ejector. In order to entrain the secondary flow, the ejector inlet shape must provide a path for the secondary flow to enter the ejector as seen in Figure 11 from (Presz, Reynolds, & Hunter, 2002). A simple rounded inlet was used in Presz which yield sufficient entrainment of a secondary stream, but it was noted that the inlet of the ejector was of great importance and needed to be redesigned



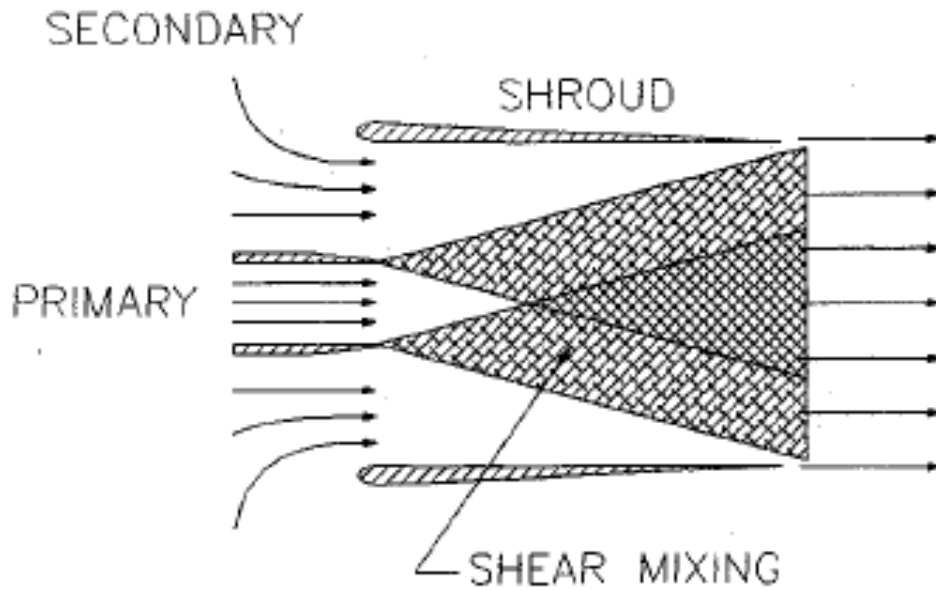


Figure 11: Ejector schematic including streamlines of primary and secondary streams and their subsequent mixing inside the ejector from (Presz, Reynolds, & Hunter, 2002)

In (Paxson, Wilson, & Dougherty, 2002) a circular lip was included to the design of an ejector which worked with a pulsejet driver. The results are shown Figure 12 and was noted by Paxson that with ejectors with high thrust augmentation the rounding is very important but does not reach a point where increasing radius no longer has an effect. This could be attributed to flow separation from a circular design. Choutapalli (Choutapalli I. M., 2007) recommended using a super ellipse profile rather than a circular profile in that a super ellipse has the added benefit of becoming flat at the junction where the ellipse and the ejector meet. This comes from the equation of an ellipse (eqn. 1.4) as  $z \rightarrow \infty$  the ellipse becomes a square.

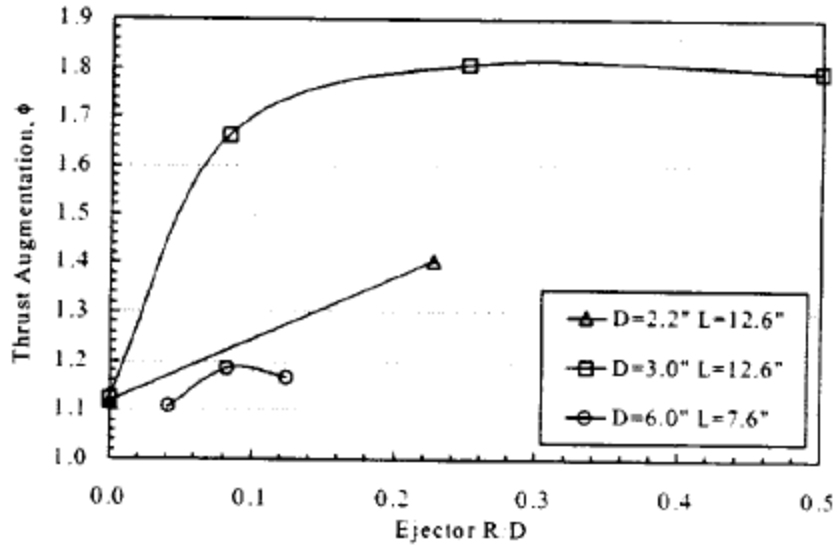


Figure 12: Thrust augmentation as a function of ejector inlet rounding for various ejector diameters and lengths with fixed distance between ejector inlet and nozzle exit from (Paxson, Wilson, & Dougherty, 2002)

$$\frac{x^z}{a^2} + \frac{y^z}{b^2} = 1 \quad (1.4)$$

### Ejector Performance Capabilities

To gain perspective on the performance increase an ejector can have on a propulsion engine an ideal ejector is investigated. In (Bevilaqua, 1987) an ideal ejector for steady flow was presented in comparison to losses the ejector may be susceptible to. The potential losses given by Belvilaqua are incomplete mixing between two streams, skin friction, separation at the inlet and other real fluid effects. Figure 13, from Belviaqua, shows an ideal ejector thrust augmentation with increasing inlet and diffuser area ratios. Figure 14 shows the effects of the losses previously mentioned where  $\beta$  represents incomplete mixing and  $h$  represents the nozzle thrust losses.

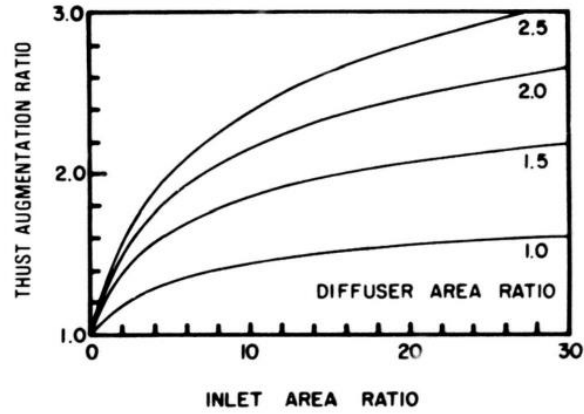


Figure 13: Thrust augmentation of an ideal ejector according to momentum theory from (Bevilaqua, 1987)

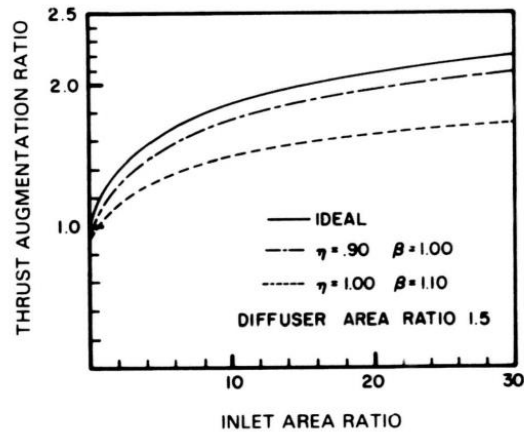


Figure 14: Effect of losses on ejector thrust augmentation from (Bevilaqua, 1987)

The results above in Figure 14 are consistent with results from other literature such as, (R.M., 1963) , (Quinn, 1973) and (Choutapalli, Krothapalli, & Alkislar, 2012) where thrust augmentation ratios for steady jets were found to be below 2.0. It is also important to note that the above-mentioned literature also found thrust augmentation ratios above 2.0 for pulse jets and PDE. This is consistent with the theory that the increased mixing due to pulses will further increase thrust augmentation but has not yet reached ideal conditions seen in Figure 14.

## Nozzle Geometries

Non-circular nozzles can help with the addition entrainment of ambient air and can theoretically provide additional thrust augmentation when its jet passes through an ejector. In (Miller, Madnia, & P., 1996) a numerical simulation was done for circular and non-circular nozzles. The non-circular nozzles included triangular, elliptic and rectangular jets with similar and dissimilar aspect ratios and similar exit circumferences. The analysis was done using Navier-Stokes equations in which the computational means was taken using a Flux Corrected Transport finite difference algorithm. An interesting axis switching phenomenon was found for geometries with dissimilar aspect ratios (ex. 2:1 of a rectangle) which therefore inhibits stream-wise vortices. Figure 15 shows a schematic for the axis switching of various geometries.

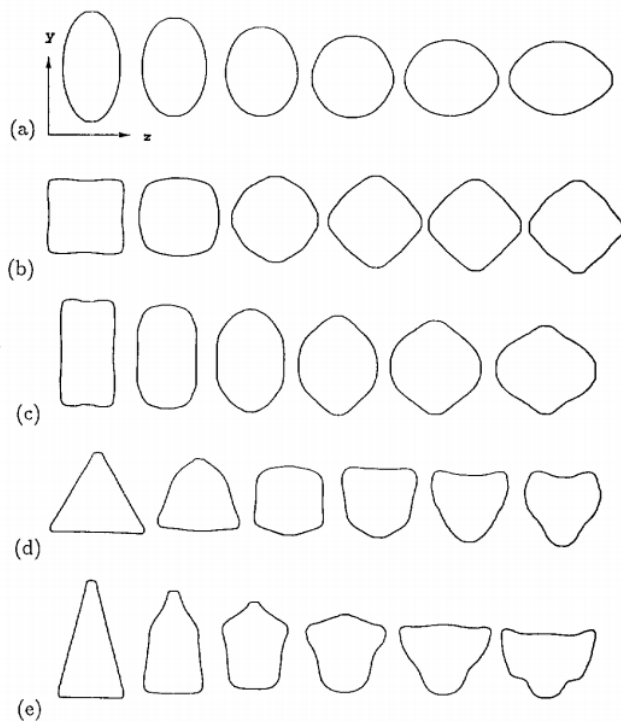


Figure 15: Axis switching of elliptic, square, rectangular, equilateral triangle and isosceles triangle from (Miller, Madnia, & P., 1996)

All the geometries in the above schematic present some form of axis switching minus the square geometry. The square geometry exhibits a rotational phenomenon. Whether axis switching or rotating all configuration were found to inhibit more mixing and entrainment of ambient air due to the vortices formed. Miller also found that the shapes with corners axis switched at approximately twice the distance compared to their smooth counterparts. This in turn shows that depending on the application when maximum mixing is desired, sharp corners or smooth corners have their advantages.

A study was also done to characterize the centerline mean flow and mixing characteristics for nine different nozzle orifices in (MI, Nathan, & Luxton, 2000). The nine nozzles consisted of ellipses, triangles, rectangles, crosses and stars. The triangles and rectangles came in differing aspect ratios as well. The experiment sought out to measure centerline mean velocity through an experimental set-up which included tungsten wire calibrated against a standard pitot-tube. The results showed that no matter the geometry, all mean velocity decayed faster than the standard circular nozzle. This faster decaying is associated with increased entrainment of secondary fluid and increased mixing. The study also found the square nozzle proved to provide the greatest mixing with the isosceles triangle, star, and cross geometries not having significant changes in mixing qualities.

### **Unsteady Thrust Generation**

The thrust generation by an unsteady jet is known to higher than that of a steady jet. The following equation help us understand why this phenomenon occurs and was developed by (Krueger, 2001).

$$F(t) = T_U + T_P = \rho \int u_j^2(r, t) \hat{n} dA + \int [p(r, t) - p_a] \hat{n} dA \quad (1.5)$$

The increase in thrust can be attributed from the formation of the vortex ring between primary flow and secondary flow. It is shown in (Krueger, 2001) that the over-pressure at the nozzle exit can be related to the additional momentum that must be provided to the formation of the vortex ring when entraining additional secondary flow. The creation of the vortex ring therefor creates an over-pressure at the exit of the nozzle which results in the higher thrust. In the equation the first term  $T_U$ , is the thrust due to the unsteady component of the velocity  $u_j^2(r, t)$ . The second term  $T_P$ , is the additional thrust produced by an unsteady jet which comes from the overpressure at the nozzle exit  $p(r, t)$ . The overall addition of the overpressure causes the jet to produce more thrust than a steady jet.

## CHAPTER II

### EXPERIMENTAL SETUP

#### **Overview**

The following chapter will go over the experimental setup for the jet turbine and the pulse jet. The experimental setup will include the instrumentation used, calibration methods of instrumentation, system components, connections, uncertainty, data acquisition system.

#### **Jet Turbine Test Stand**

The Aerodynamics and Propulsion Laboratory at the University of Texas – Rio Grande Valley houses a jet turbine test stand (JTTS) able to characterize a hot flow turbine (Figure 16). The JTTS measures 2 ft in width 5 ft in height and 5 ft in length. The JTTS is constructed out of 1-inch steel tubing and was welded together to form the frame. The test section measure 2ft in width 1.5 ft in height and 5 ft in length and is encased by plexi-glass on the sides. The JTTS houses a JetCat 180 RXi jet turbine capable of speeds up to Mach 1 and thrust of 40 lbs. The Jet turbine sits on a linear axial plate inside of the test section which impinges upon a load cell to measure the thrust performance. A Pitot probe is positioned aft of the turbine and is used to measure total and static pressure and subsequent velocity and Mach of the jet turbine. The pitot probe is held by a mechanism able to move in both the axial and traverse direction to allow for sufficient

measurements of the jet profile. A J-type thermocouple is also held by the pitot traversing mechanism. The JTTS has the ability to roll out of the facility onto the test platform outside for



*Figure 16: Jet Turbine Test Stand (JTTS)*

safe testing as to not cause harm due to the fumes of the exhaust jet. The JTTS also has a breaking system using floor lock to prevent from movement of the JTTS during testing

### **Jet Turbine**

The jet turbine used in this study is a JetCAT P180-RXi. This turbine is a model turbine primarily used as propulsion engines for model aircraft. The jet turbine is capable of 40 lbs. of thrust at the max rpm of 125,000 which also produces temperatures of 730°C (1346°F). The overall range of rpm is 33,000-125,000. The overall dimensions of the turbine are 4.4 inches in diameter and 13 inches in length. The turbine consists of a single compressor which leads compressed air into a



combustion chamber where a fuel/air mixture is ignited. A single turbine then expands the air in the converging nozzle which is expanded into the ambient air.

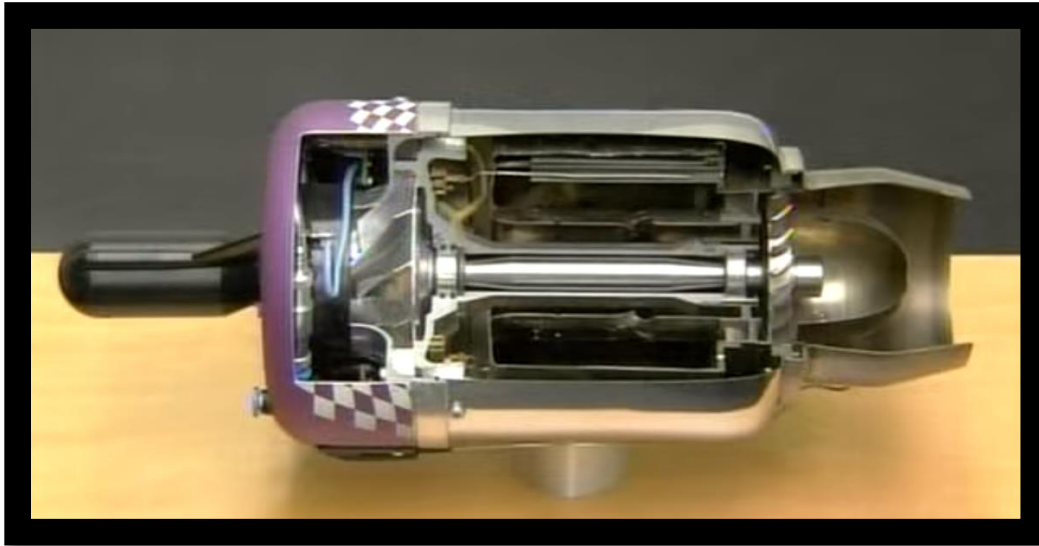


*Figure 17: JetCAT P180-RXi internal view*

The jet turbine comes equipped with many external connectors including BUS channels for remote control capabilities. The LED I/O Board (Input/Output) is a connection point for the data bus and a display for the current status of The Electronic Control Unit (ECU). The ECU serves as the unit which electronically turns on and off the different function of the turbine. The ECU is connected to the LED I/O Board, power supply and the Ground Support Unit (GSU). The power supply used is a BK Precision 1901 B switching mode power supply capable of 1-32VDC and 30A. For the turbine 9.9V and 15A are required. The GSU serves as the terminal for displaying and programming parameters such as rpm, run time and exit gas temp (built in thermocouple). The primary use of the GSU for the purposes of this study is to monitor and change rpm parameters.

## Pressure Measurements

Pressure measurements were taken using Omega PX313-50PSIA series pressure transducers with MINI DIN connector. The pressure transducers use a high-accuracy silicon sensor protected by an oil-filled stainless-steel diaphragm. Two pressure transducers were used for this study with a range of detection of 0-50 psia, an excitation voltage ranging from 0 to 30 Vdc and an output of 0–5Vdc. The Omega pressure transducers have an accuracy of which includes combined linearity, hysteresis and repeatability of  $\pm 0.25\%$  BSL, max. Pressure transducers were calibrated using an Omega PCL819 Pressure Calibrator. The pressure calibrator uses an internal electrical pressure pump capable of creating a vacuum or pressures ranging from -12 to 300 psig with an accuracy of 0.025% full scale (FS).

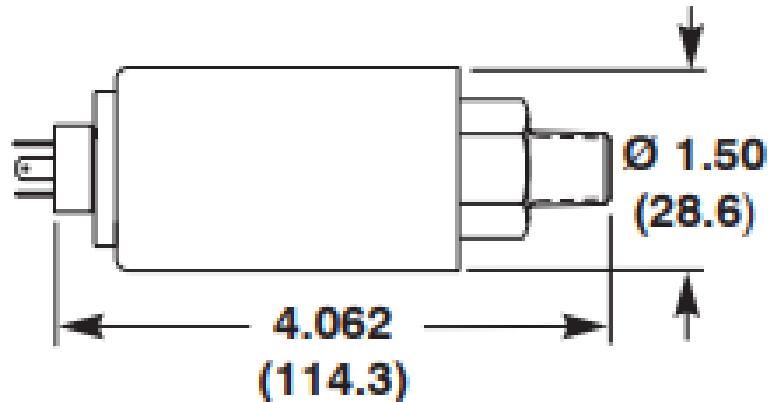
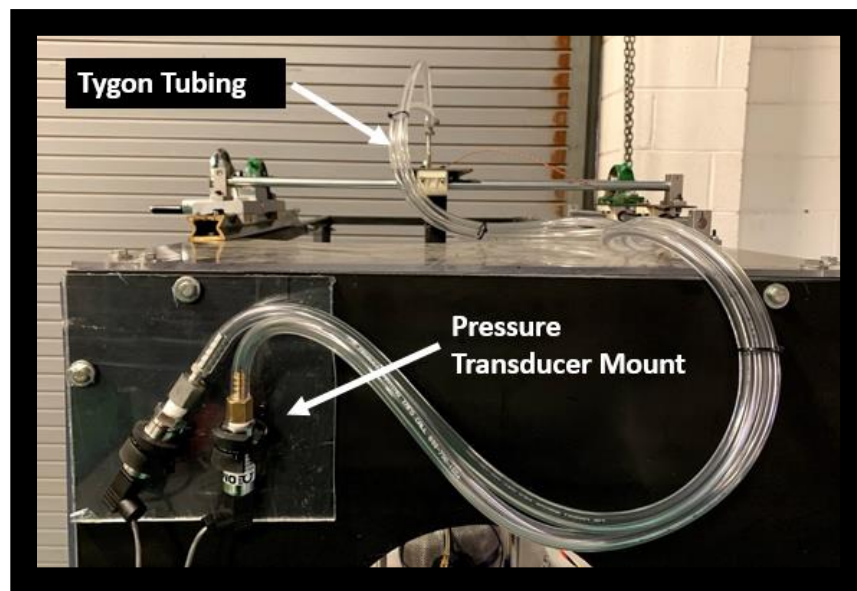


Figure 18: Omega PX313 series pressure transducer



*Figure 19: PX313 calibration on PCL819 device*

The calibration method included the vertical mounting of the pressure transducer onto the calibration device. A known pressure was stimulated from the calibration device in which the pressure transducer outputted a voltage which was recorded on LabVIEW. Five different known pressures and output voltages were recorded and transformed into a calibration curve.



*Figure 20: Front plate pressure transducer mount*

Once calibrated the pressure transducers were mounted on the front plate of the JTTS covered by a plexi-glass (Figure 20) as it was found that this installation prevented external electric

interference. Both pressure transducers were connected to a pitot probe through tygon tubing. One pressure transducer was used to measure stagnation pressure while the other was used to measure static pressure. A pitot probe (Figure 21) measures stagnation pressure which is depicted here as  $P_2$  and measure static pressure depicted as  $P_1$ . The differential pressure correlated to an induced velocity in the flow in which a subsonic compressible flow formula is used to calculate for Mach.

$$M = \frac{v}{a} = \sqrt{\frac{2}{\gamma-1} \left[ \left( \frac{P_{Stagnation}}{P_{Static}} \right)^{\frac{\gamma-1}{\gamma}} - 1 \right]} \quad (2.1)$$

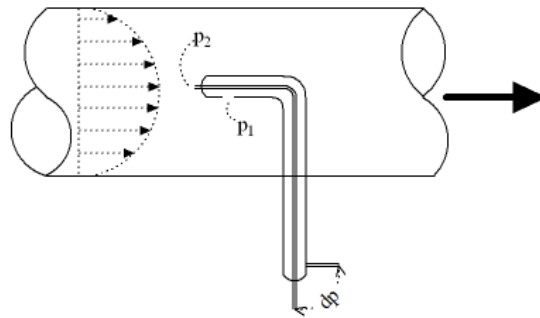


Figure 21: Schematic of pitot probe

In order to fully characterize the pressure field aft of the jet turbines exit gas, a pitot traversing mechanism Figure 22, was implemented onto the JTTS. The pitot traversing mechanism is mounted aft of the turbine to which the nose of the pitot probe inlet sits directly at the center of the nozzle exit. The pitot rack can traverse in the axial direction with the utilization of a rack and pinion system. The traversing mechanism can also move in the lateral direction using a threaded rod put through two bolts which supports the carriage that holds the pitot probe.



*Figure 22: Plot traversing mechanism*

## **Force Measurements**

To characterize the thrust produced by the jet engine an Omega LC302-50 load cell (Figure 22) was used. The load cell is a stainless-steel compression, push button load cell which uses high accuracy strain gages to measure force. The load cell is capable of measuring loads of 50 lbs. with a maximum overload of 300% of capacity. The load cell has an excitation voltage of 10Vdc and output of 1mV/V while having a linearity, hysteresis and repeatability combined accuracy of  $\pm 0.5\%$  FSO. The load cell is mounted in front of the axial traversing plate which carries the jet engine and can be seen on figure 24. A threaded rod impinges on the load cell while in use as to directly measure the thrust produced from the jet engine.

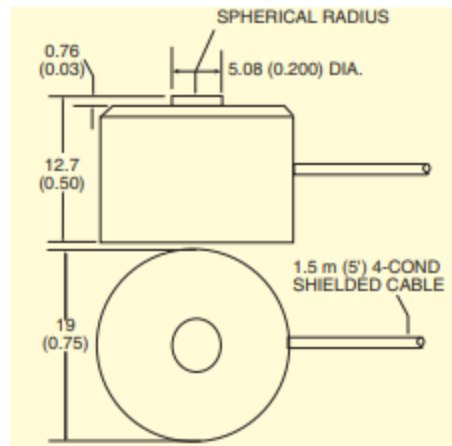


Figure 23: LC302-50 schematic

To calibrate the load cell a direct measurement was taken with the assistance of a system of pulley wheels and a steel cable (Figure 25). Known loads were placed at the end on a platform of the steel cable causing the load cell to produce a voltage output which was recorded to LabVIEW. Like the pressure transducer calibration, five point were taken and turned into a calibration equation.

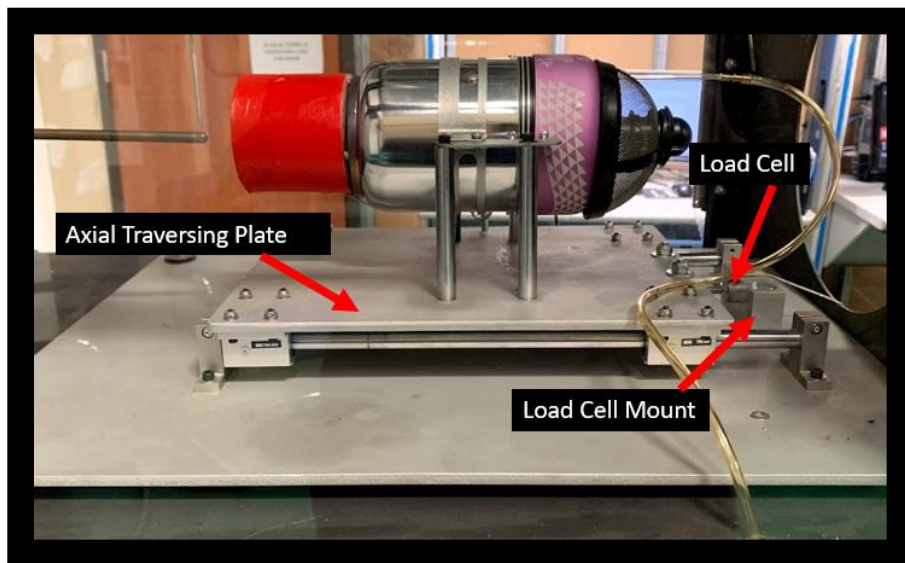
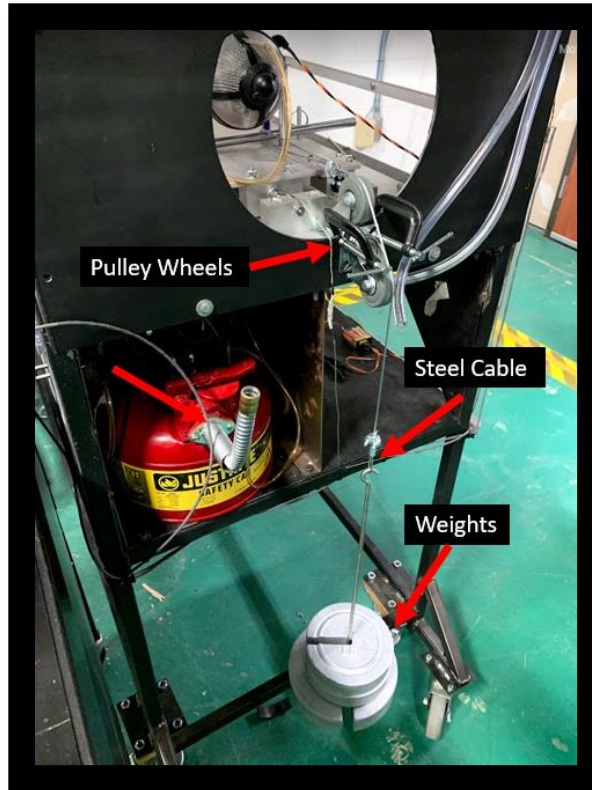


Figure 24: Thrust measurement technique



*Figure 25: Load cell calibration technique*

## **Temperature Measurements**

To characterize the temperature field aft of the turbine while in use an Omega J-type thermocouple was used. The thermocouple utilizes dissimilar electrical conductors which forms an electrical junction at different temperatures which produces a voltage output which can be calibrated to measure temperature. In the case of J-type thermocouples the two dissimilar conductors are Iron and Constantan with the ability to measure temperatures of up to 800°C. The use of Omega thermocouples with National Instruments DAQ systems come self-calibrated for type of thermocouple. Small changes in CJC factor in the LabView program were adjusted based on the calibration technique of dipping the thermocouple in ice water (corresponds to 0°C) and

then dipping the thermocouple in boiling water (corresponds to 100°C) to get known upper and lower temperature readings.

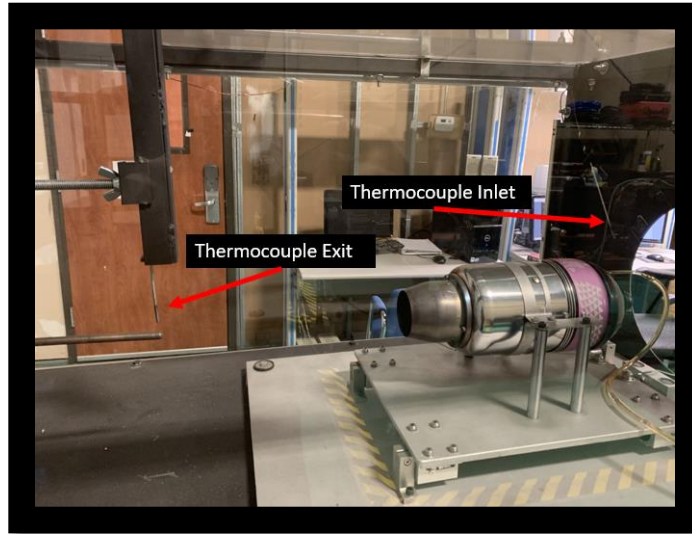


Figure 26: Inlet and exit thermocouple placement

**Wiring/Connections**

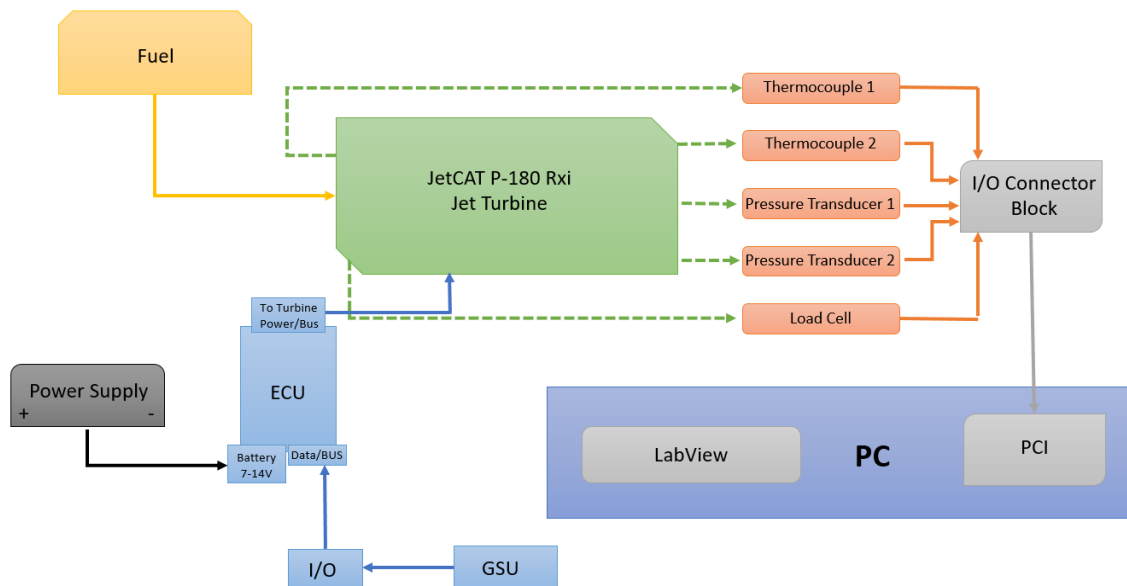


Figure 27: Block diagram of JTTS system



The wiring of the various instrumentations and turbine control units are shown in the block diagram in the above Figure. As discussed earlier the GSU, I/O and the ECU act as the combined control interface between the turbine and the user. The interface and initial start-up of the turbine are powered by a power supply which replaced the original rechargeable battery giving the user better opportunity for consistent runs. The fuel system, Figure 28, is comprised of a 1gallon steel tank in which a fuel line is run up to a shutoff switch mounted on the side of the JTTS for emergency cutoff situations. The fuel line is then run to the jet turbine where the fuel line is reduced in diameter through a coupling to fit into the jet turbine intake. The fuel system also has a built-in priming mechanism which utilizes a hand pump to allow for adequate fuel supply upon startup of the jet turbine.

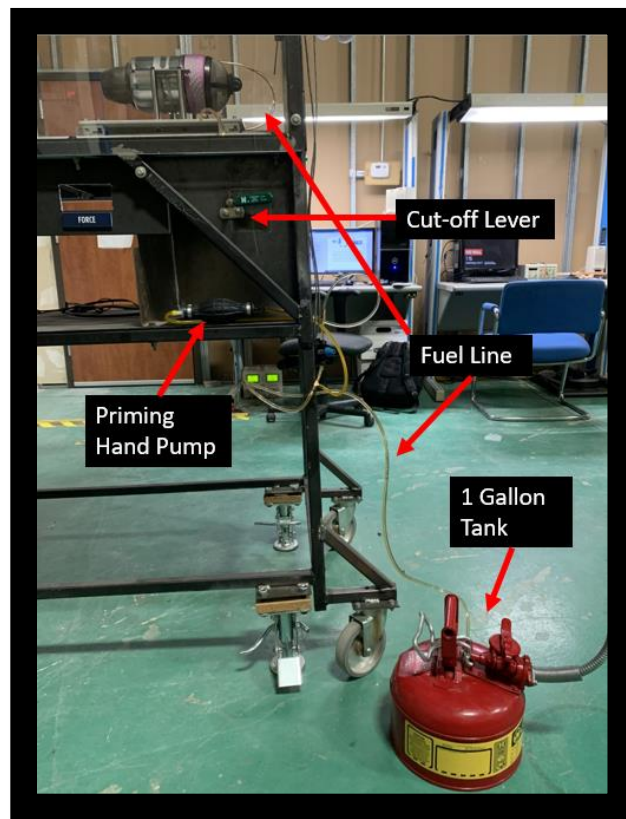


Figure 28: Fuel System

The instruments (thermocouples, pressure transducers and load cell) are stationed around the turbine to fully characterize the engine.

### **Data Acquisition**

The process of collecting data for this study was done by utilizing a data acquisition system or DAQ. The DAQ in this case is comprised of a National Instruments SCB-68 I/O connector block, National Instruments PCI-6250 (DAQ card) and a LabVIEW code. The connector block interfaces I/O signals, in this case the from instrumentation mentioned before, to the DAQ card. The connector block is an M series shielded 68-pin connector which transfers voltage signals while helping with noise signal termination. The voltage signal is then passed to the PCI-6250 or DAQ card which is an M series device that converts analog signals to digital signals. The DAQ card is a 16 analog input device which uses an NI-PGIA amplifier which allows for fast settling time and at high scan rates. This is especially useful when collecting data from several instruments. A LabVIEW program was created to read the digital signals from the DAQ card in real time and in an efficient and accurate manner. The LabVIEW program played two roles, as the GUI which displays real time figures such as pressure, temperature and thrust reading and as the program which collected and stored data for processing. Two important parameters that are essential to data collection is the rate at which data is collected and the number of samples taken. The sampling rate for this study was chosen to be 125,000 Hz. The high sampling rate assures that sampling will include accurate data. The number of samples for the study was chosen to be 40,960 samples per channel to coordinate with the bin collection method of the computer.

A MATLAB code was also developed to process the data which was saved in .dat file types from LabVIEW. With the utilization of for loops the MATLAB code imports the data from the

various files and arranges them in an array of cells in which they are then converted into  $N \times 1$  matrix where  $N$  is the number of samples. Each column then represents the number of samples at a specific time for each of the five different instruments. Averages are then taken for each column and used as a single data point. The data points are collected, and plots are made for visualization of experimental results.

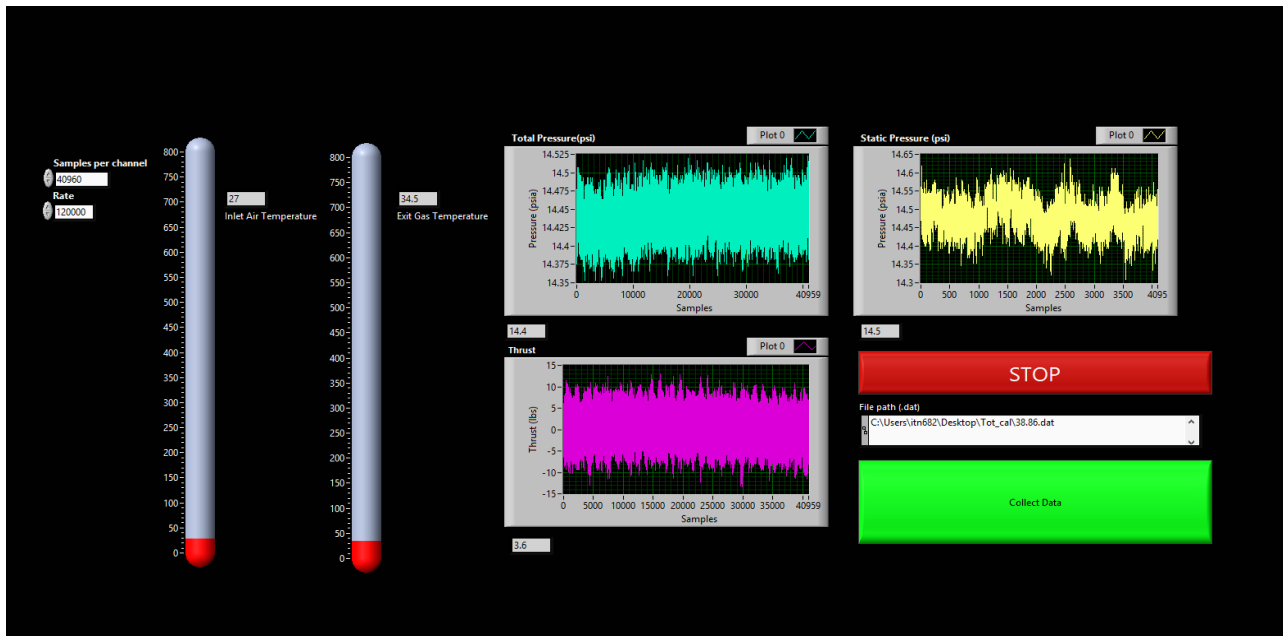


Figure 29: Graphic user interface of LabVIEW code

### Pulse Jet Ejector Thrust Augmenter

The Aerodynamics and Propulsion laboratory also houses the Pulse Jet Ejector Augmenter or PETA that is described in (Choutapalli I. M., An Experimental Study of a Pulsed Jet Ejector, 2007). The PETA is a cold flow jet which utilizes a flow chopper to create pulses in the jet. PETA can be run as both a steady cold jet and as a pulsed cold jet. The PETA is comprised of an inline flow which intakes high pressure air from a compressor housed outside the facility. The air is then

fed to a stagnation chamber in which a rotating disk chops the pressurized air and generates the pulsed flow. The pulsed flow then passes through a nozzle and is expanded to a 2D ejector. A flexible joint exists between the stagnation chamber and the nozzle which allows for the backwards movement of the nozzle. Linear bearing utilizes this movement and impinges upon a load cell which reads thrust results. During experimentation the PETA can be run with and without the ejector in order to record results for thrust augmentation. The PETA has already been proven to produce thrust augmentation ratio results upwards in the range of 1.8 when running under an area ratio of 11 in a pulsed jet case. The purpose of including the PETA is to further advance studies on asymmetric nozzle shapes and its effects on thrust augmentation through an ejector which will be described in subsequent sections. The different components of the PETA will be discussed in the following section limited to the knowledge needed to know for this specific study as the detailed specifications for the PETA system can be found in (Choutapalli I. M., An Experimental Study of a Pulsed Jet Ejector, 2007).

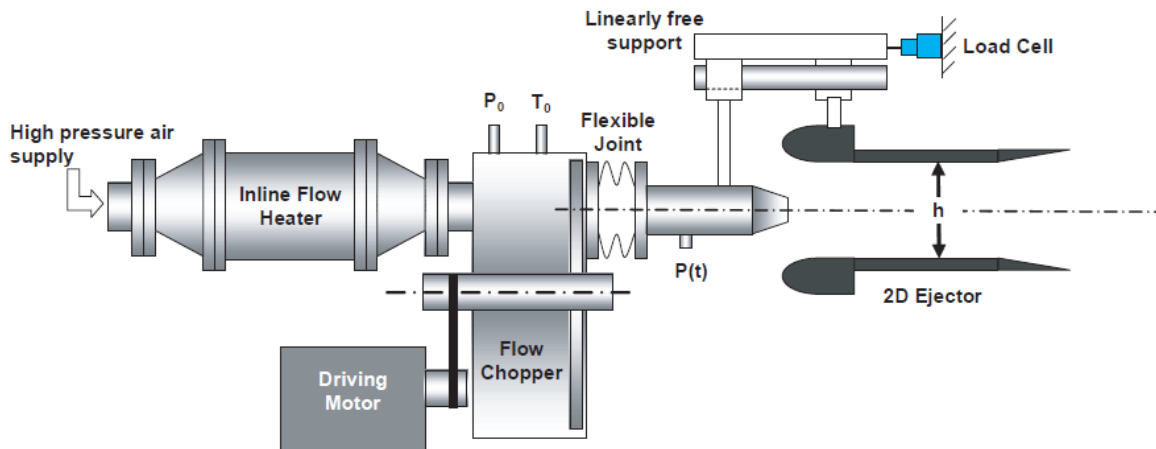


Figure 30: Schematic of Pulse Jet Ejector Augmenter from Choutapalli, 2007

## **Instrumentation**

The PETA uses Omega pressure transducers similar to the ones described for the JTTS with the exception of pressure ranges and are of gauge type. An Omega PX309-1KG5V pressure transducer reads the pressure from the compressor before the air leads into the pressure valve. The pressure transducer differs from the transducers mentioned for the JTTS in that its operating range is 0-1000 psi gauge and uses silicon strain gages molecularly bonded to the stainless-steel diaphragm to accommodate for the higher pressure. An Omega PX309-030G5V reads the pressure from the stagnation chamber which has a range of 0-30psig and an Omega PX309-015G5V pressure transducer reads the pressure from the nozzle. All pressure transducers mentioned in this section have an accuracy of which includes combined linearity, hysteresis and repeatability of  $\pm 0.25\%$  BSL, max. All pressure transducers in use on the PETA were also calibrated using the technique mentioned in the Pressure Measurements section of the Jet Turbine Test Stand and have a voltage output of 0-5V. An Interface 1500ASK-100 load cell is used to measure thrust of thrust balance. The load cell is a push button load cell capable of reading loads up to 100lbs. The load cell has a static error band, nonlinearity and hysteresis each of  $\pm 0.05\%$ , Non-repeatability of  $\pm 0.02\%$  and an eccentric load sensitivity of  $\pm 0.25\%$ . The load cell was calibrated using the technique mentioned in the force measurement section of the JTTS. A k-type thermocouple is used to measure the temperature in the stagnation chamber. The k-type thermocouple consists dissimilar wires which produce a linear voltage difference used to read temperature. All Omega thermocouples come self-calibrated when read through a Nation Instruments device.

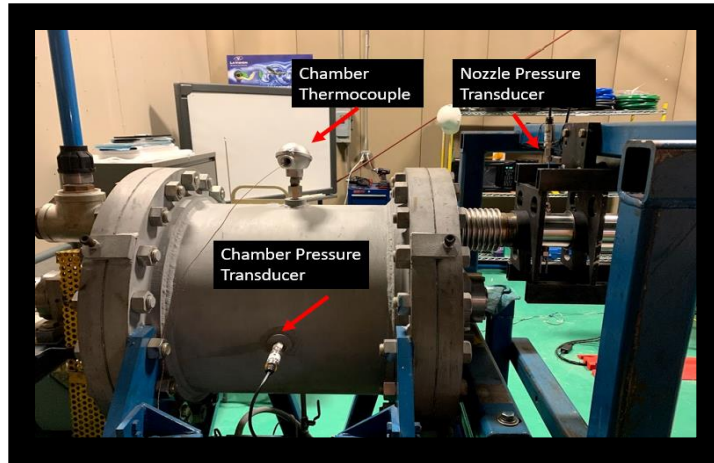


Figure 31: Chamber thermocouple, pressure transducer and nozzle pressure transducer placement



Figure 32: load cell placement within thrust balance

## Air Supply

The air supply for the Pulse Jet comes from an Ingersoll Rand air compressor coupled with an air compressor dryer and an air compressor filter. The air compressor is capable of pressures of up to 115psi during run times. The dryer is used to remove moisture from the air that can cause damage to the air system. The filter is used to remove contaminants such as oil or dust particles for a clean stream of air. The highly pressurized air is then fed into the facility and through a pressure valve. The pressure valve is the primary source of which the flow is controlled to allow

for the proper air stream velocity. The pressure valve is connected to the PC used for experimentation in which the actuator of the pressure valve is opened at a certain percentage of full actuation that is calibrated to correspond to a certain pressure of wanted Mach numbers. There also exist a shut off valve between the air compressor and the pressure valve that is activated when the system is not in use or in emergency situations.



*Figure 33: Pressure valve system*

### **Flow Chopper**

The flow choppers purpose in the PETA system is to create the pulsed flow from the highly pressurized air in the stagnation chamber. The flow chopper is a rotating disk that is housed inside the stagnation chamber nearest the capped wall that leads to the nozzle. The flow chopper has six equidistant holes with diameters that match the diameter of the exit duct that leads to the exit nozzle. Since the flow chopper cannot be placed directly next the that capped wall due to friction concerns, a Teflon seal is attached to the flow chopper with the same geometry as the chopper to prevent air leakage. The flow chopper is controlled by a Baldor CSM3615T-2 DC motor which

rotates the chopper through a series of belts and bearings in which a shaft connected to the center of the chopper sits on. DC motor is controlled by is associated handheld controller in which desired frequencies can be inputted. The rotational speed or rpm of the flow chopper can be found by taking the frequency, multiplying by 60(minute factor) and dividing by 6 (number of holes).

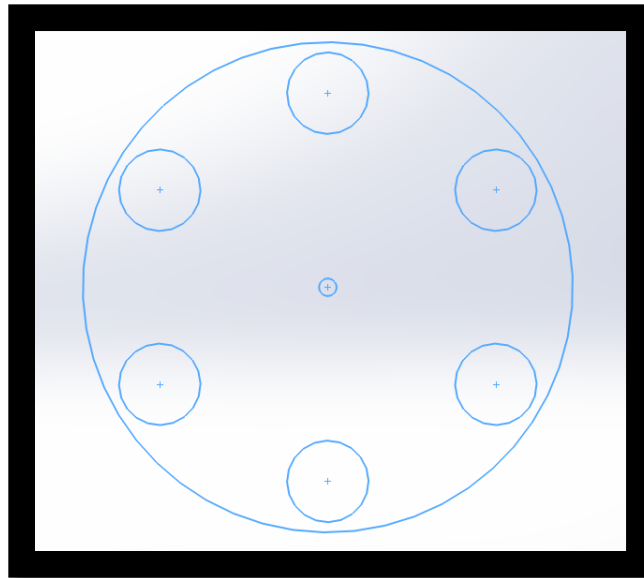


*Figure 34: Schematic representation of flow chopper*

### **Direct Thrust Measurement System**

The direct thrust measurement system or thrust balance utilizes a system of roller bearing which sit on cylindrical rods to promote the axial movement of the thrust balance to impinge upon a load cell to measure thrust. The roller bearings are attached to the thrust balance framework which is fastened to the nozzle/nozzle duct/flexible joint and the ejector assembly. As mentioned earlier when the pressurized air passes through the flexible joint and ultimately is expanded out of the nozzle, thrust is created in a backwards axial direction due to the extension of the flexible joint and the coupled sliding of the bearings. This creates the movement which allows for the impingement of the load cell and is deemed as a direct thrust measurement. The thrust balance is



calibrated using the same technique mentioned in the force measurement section for the JTTS. Using the technique of adding known weights and measuring voltage outputs of the load cell and calculating the systems subsequent calibration curve gives the advantage of taking into account friction forces of the bearings and the compression force of the flexible joint.

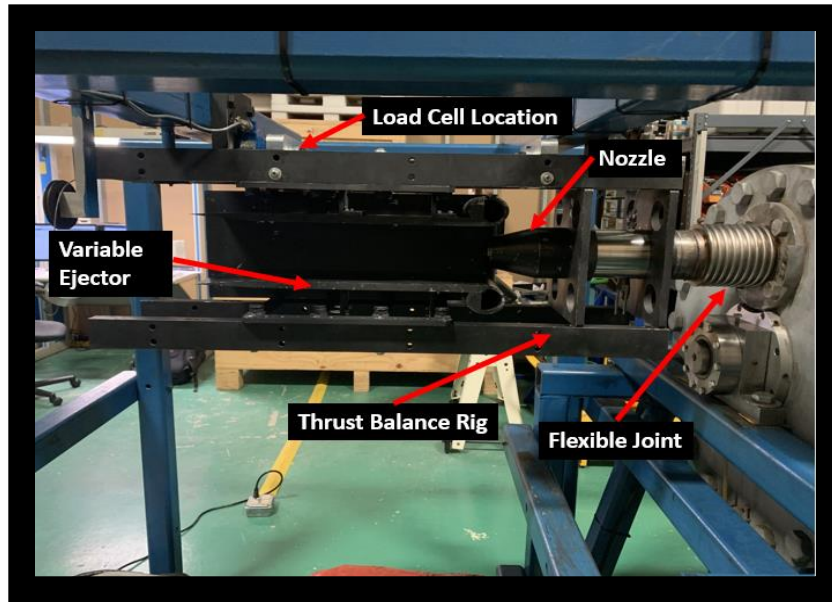


*Figure 35: Direct thrust measurement system*

### **PETA Ejector**

The ejector used for the PETA is a 2-D rectangular ejector which measures 508mm in length, 150mm in width and has a variable height of 38.1mm – 158.75mm. The variable height allows for different area ratios to be tested. The ejector is part of the direct thrust measurement system so thrust measurements are easily obtained when the ejector is on. The ejector utilizes a super ellipse as the inlet lip that entrains ambient air. The super ellipse design fosters proper entrainment of ambient air so that flow separation at the inlet does not occur. This is because the super ellipse at the junction between the ellipse and the inner ejector wall becomes linear. The ejector also has a divergent section nearing the end of the ejector wall to better recover the pressure before expanding

out of the ejector. The ejector length is set at 10 times the diameter of the nozzle to allow for exit flow to reach isentropic conditions. The area ratio (AR) is defined as the area of the inlet of the ejector over the area of the nozzle exit. Based on literature from Choutapalli, three AR of 7.6, 11 and 12 will be used for experimentation.

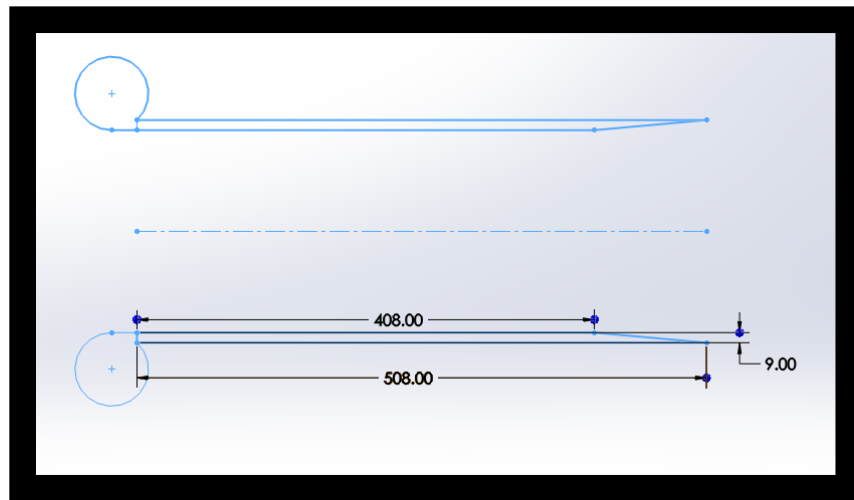


Figure 36: Schematic representation of PETA ejector

### Asymmetric Nozzles

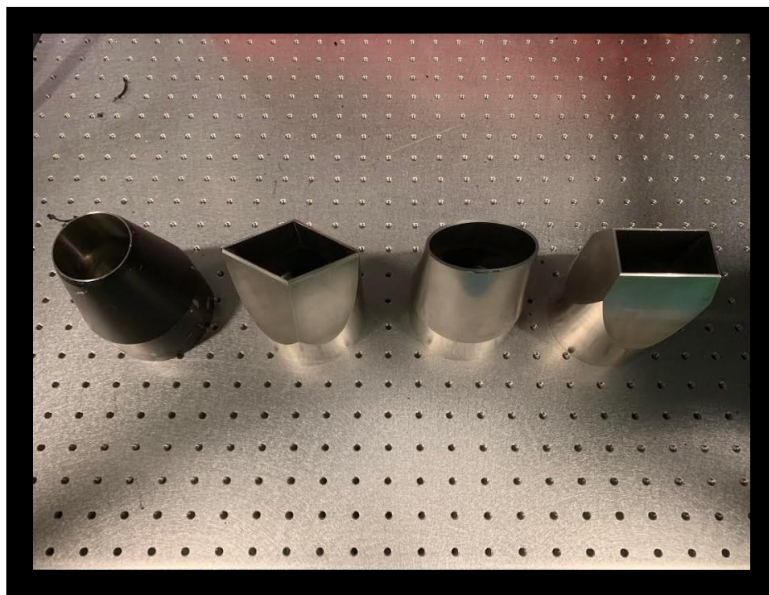


Figure 37: Asymmetric nozzles from left to right; circular, diamond, ellipse and rectangular

Four Asymmetric nozzles are tested through the various steady and unsteady cases on the PETA. The asymmetric nozzles can be identified by their exit area shape and are circular, diamond, elliptic and rectangular (Figure 37). The diamond, ellipse and rectangular nozzles all have an aspect ratio of 2:1. The hydraulic diameter is the same for all four nozzles which gives us a means to be able to study and compare the nozzles to one another.

### Wiring\Connections

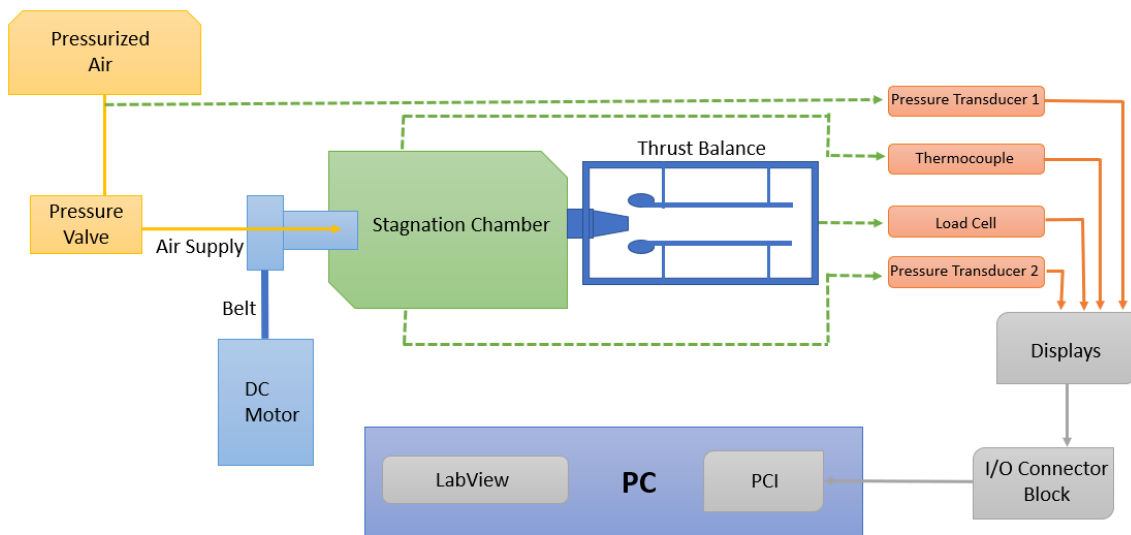


Figure 38: Block Diagram of PETA system

The wiring of the various instrumentations, air supply path and motor arrangement are shown in the block diagram in the below Figure. As mentioned before, the pressurized air passes through a pressure valve, which controls air speeds, and into the stagnation chamber. The stagnation chamber houses the flow chopper which is mounted at the wall closest to the nozzle exit. The flow chopper is powered by the DC motor which is connected to one another through a belt system. The pulsed flow is expanded out of the nozzle and through the 2-D ejector. This causes the thrust balance to move in the axial direction to impinge upon the load cell. During experimentation all instruments read their respective measurements which are then transferred and

shown on individual displays for monitoring. The information is then passed to the I/O connector block which is connected to the PCI inside the PC. A LabVIEW code was created to control the pressure valve, display values real time and save data.

### Data Acquisition

The process of collecting data for this study was done by utilizing a DAQ system similar to the one established for the JTTS. Pressure transducers and the load cell are connected to Omega DP41 Series digital panel meter displays which provide the excitation voltage that powers the instrument itself. Built in smart filtering helps suppress noise from voltage readings which is then outputted to the I/O board. The I/O board is again an SCB-68 I/O connector block that was utilized



Figure 39: Digital displays collected on a single panel

for the JTTS. The I/O board passes the voltage information along to the National Instruments PCI-6250 (DAQ card) which is read through a LabVIEW program. The LabVIEW program reads voltage values real time and displays them through various charts. The LabVIEW code is also used to control the pressure valve by changing the percent in which the actuator is open. For the PETA experiments a sampling rate of 125,000Hz was chosen while the number of samples read was

102400. The LabVIEW program also saves the data to be processed through a MATLAB code in which similar processing techniques are used to display the data from the JTTS experiments.

### Load Cell Calibration

To calibrate the load cell a direct measurement was taken with the assistance of a system of pulley wheels and a steel cable (Figure 40). Known loads were placed at the end on a platform of a steel cable causing the load cell to produce a voltage output which was recorded to LabVIEW. The know values along with their now known voltage output are plotted and a calibration equation is made.

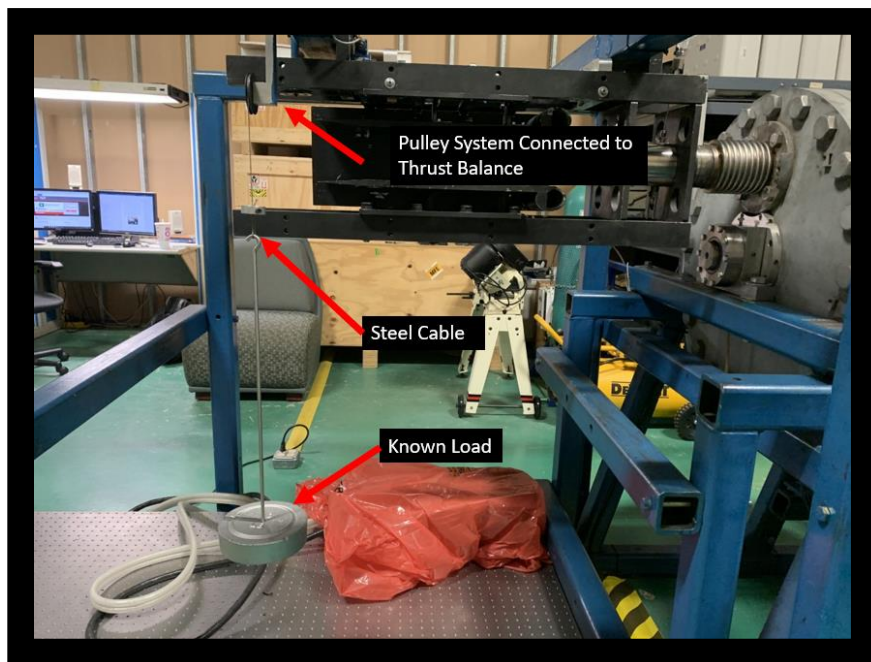


*Figure 40: Thrust balance calibration method which includes a pulley system used to measure known loads.*

## CHAPTER III

### STEADY HOT JET

#### Overview

The following results serve to characterize the performance spectrum of the jet turbine. With the characterization of the jet stream a better understanding of potential ejector performance and placement can be had. Various tests were done to measure pressures, thrust and Mach values. The following figure establishes an axis of reference.

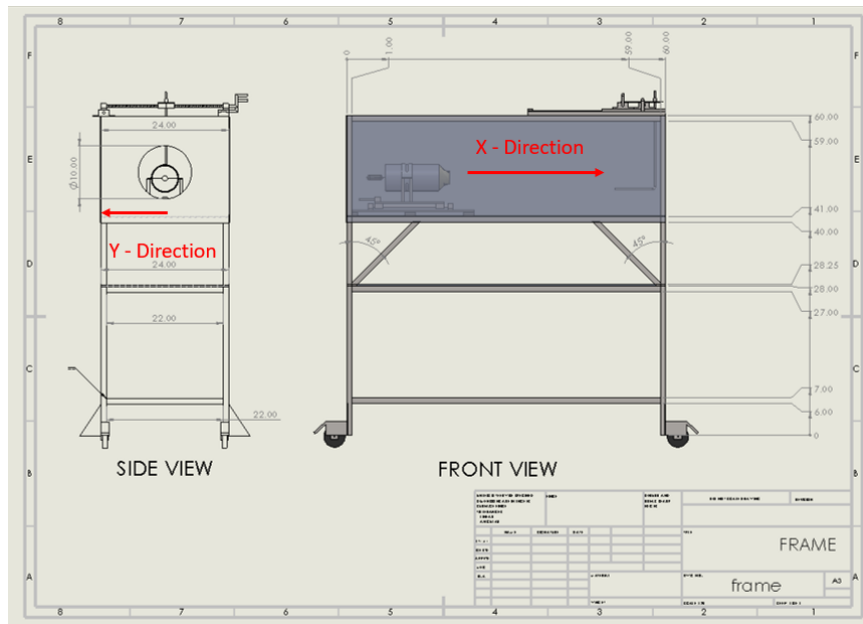


Figure 41: Jet turbine directional establishment

## Jet Turbine Characterization

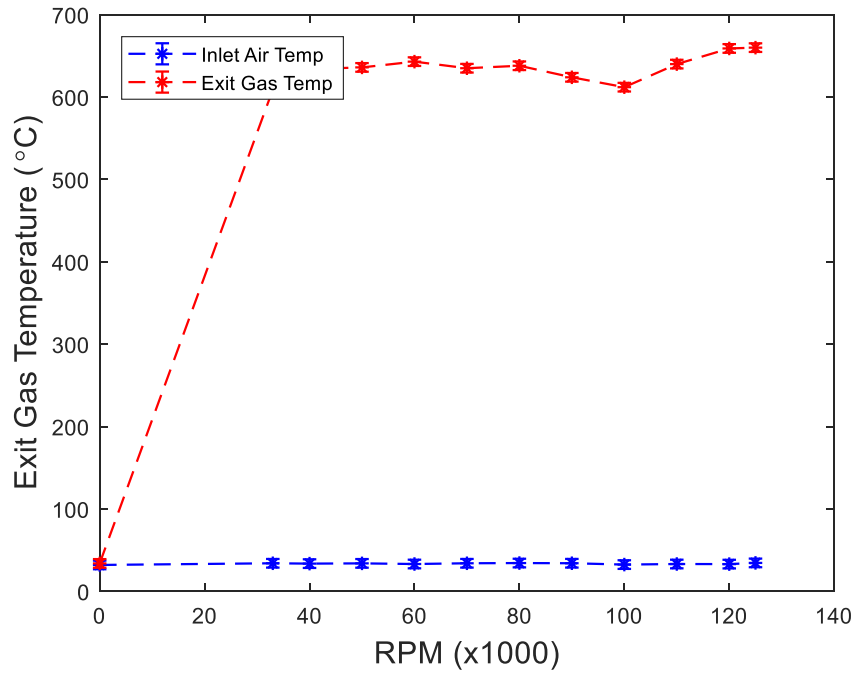


Figure 42: Exit gas temperature as a result of increasing RPM at nozzle exit

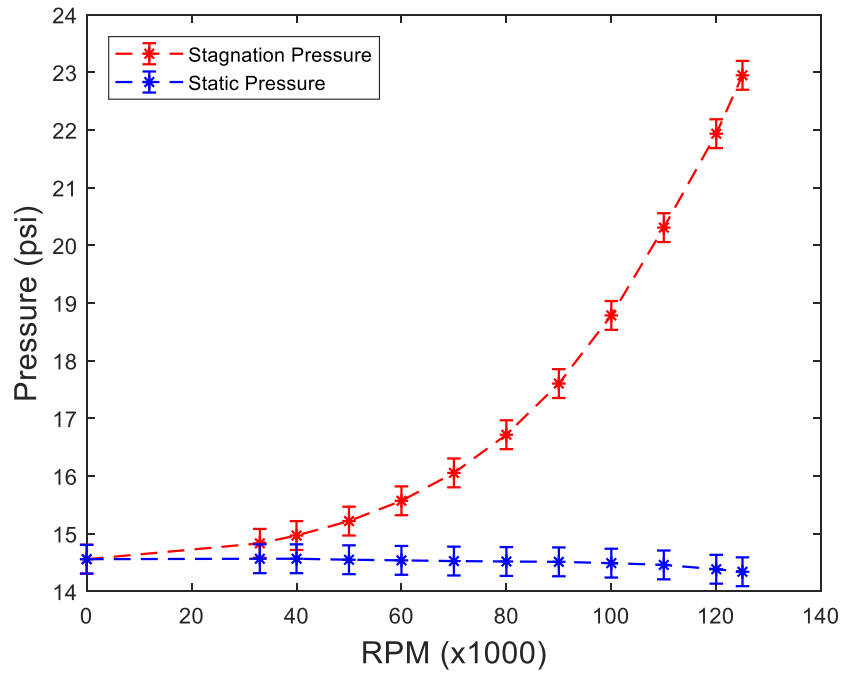


Figure 43: Pressure at exit of nozzle as a result of increasing RPM

Figure 42 shows the exit gas temperature at the center nozzle of the jet exit. As may have been expected the immense heat of the expanding gas raises to temperatures above 600C as rpm increases. The pressure in Figure 43, compares the stagnation pressure and the static pressure of the exit gas as rpm increases. The stagnation pressure steadily increases as the rpm increases and becomes more rampant at rpm of 100,000. In comparison the static pressure remains steady but has a slight drop off at 100,000 rpm. This drop off together with the increase in stagnation pressure is evidence of a transfer from the subsonic regime to the sonic regime

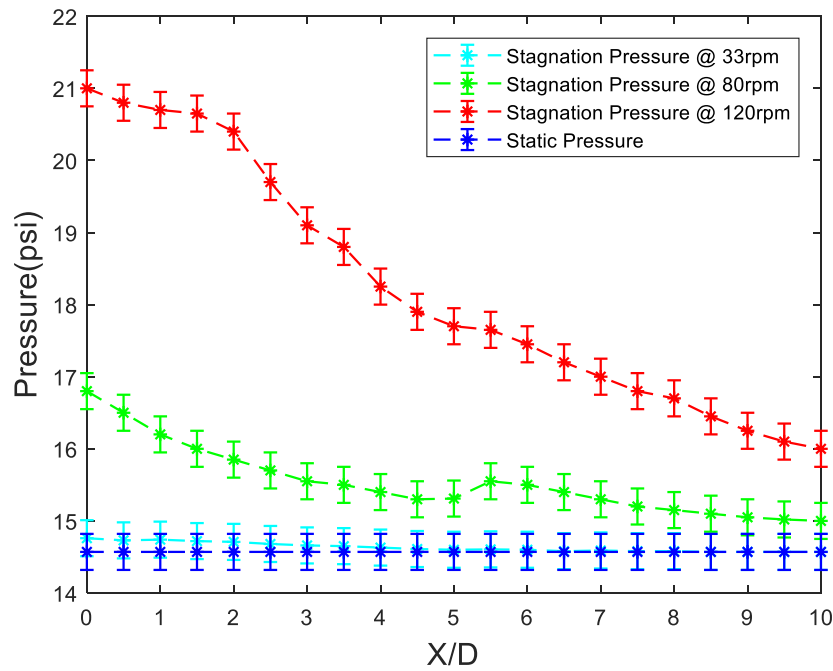


Figure 44: Pressure taken at 33,80 and 120 RPM with increasing axial distance

Pressure readings were taken at increasing axial distance from the exit nozzle to characterize the jet stream and are shown in Figure 44. Rpm values of 33,80 and 120 were chosen for the experiments as they attribute to low medium and high rpm values. The stagnation pressures at all rpm follow a general decrease as axial distance increases. Pressure readings from 80 and 120 rpm never fully recovers to ambient conditions as can be seen when comparing to the static



pressure reference and is a valuable result when thinking of the design and placement of the future ejector. The stagnation pressures at 33 rpm on the other hand recovers rather quickly at around a value of  $X/D = 4.5$ . At 120 rpm the first five values are clustered around similar pressure readings before steadily dropping off. This may be due to a larger core of the exit gas jet stream that exists compared to the two other rpm trends.

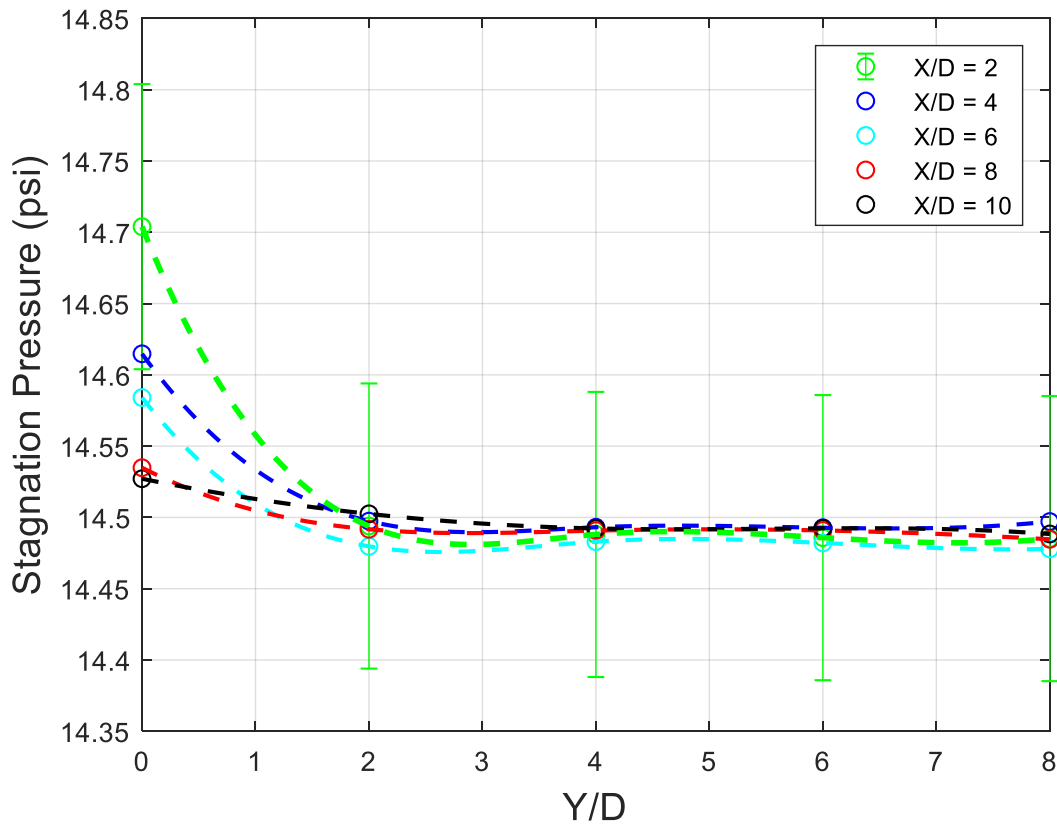


Figure 45: Stagnation pressure taken at 33RPM with increasing lateral distance at different axial distances

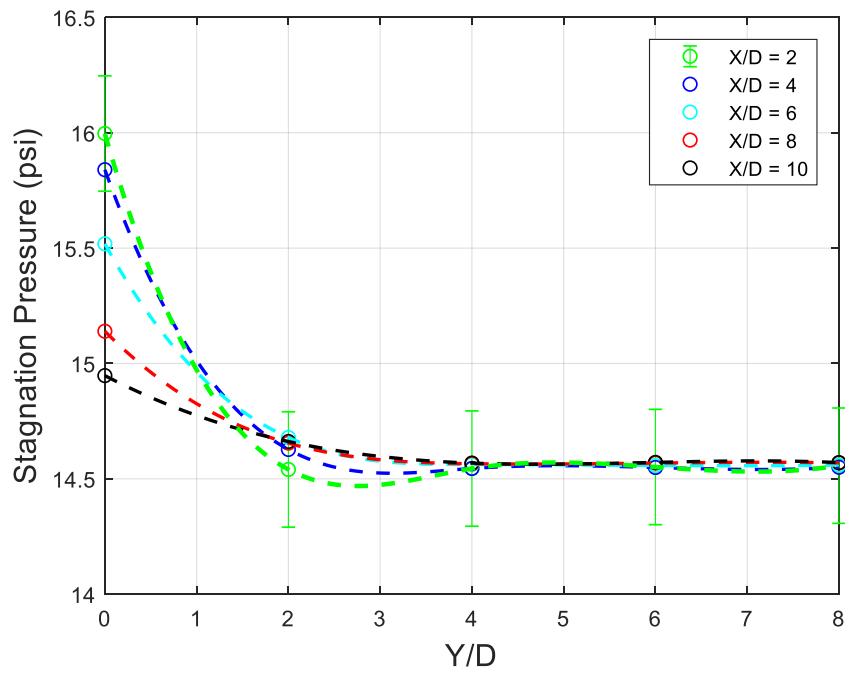


Figure 46: Stagnation pressure taken at 80RPM with increasing lateral distance at different axial distances

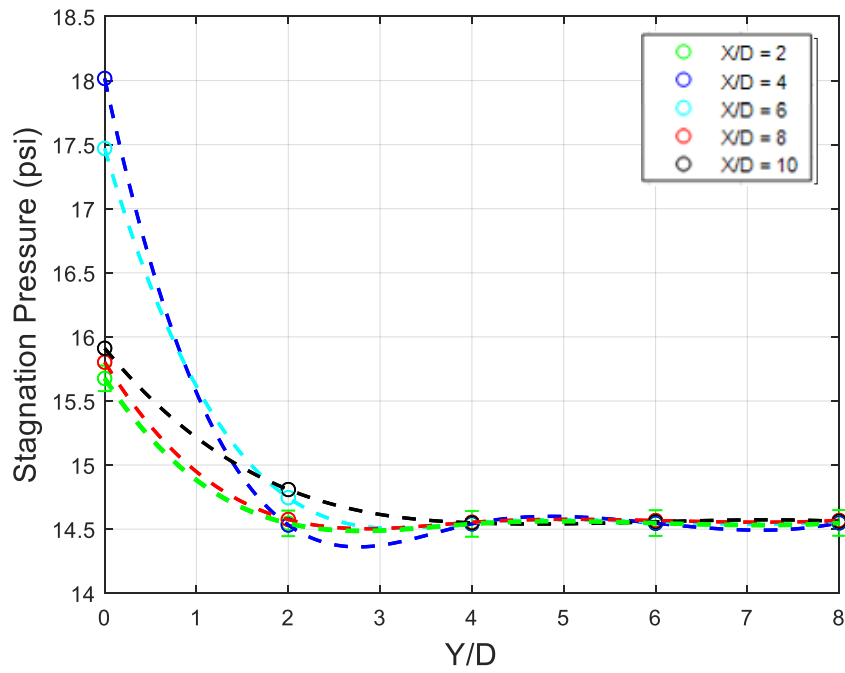


Figure 47: Stagnation pressure taken at 120RPM with increasing lateral distance at different axial distances

Figures 45, 46 and 47 represent stagnation pressures at 30,80 and 120rpm respectively. Each figure displays stagnation pressure lateral movement  $Y/D$  taken at increasing axial distances  $X/D$ . As is expected each figure presents stagnation pressures following a decreasing trend as the probe moves out of the jet stream and the pressure is fully returned to ambient conditions. For all  $X/D$  cases in Figure 46 the pressure almost immediately returns to ambient conditions due to a relatively small exit jet. Figure 46 and 47 follows the same downward trend but does not immediately return to ambient conditions except for the case of  $X/D = 2$  which tells us the probe has already exited the jet stream at this location or that the jet is slightly over expanded at the exit of the nozzle. To prove the jet is slightly over expanded PIV flow visualization must be done in the future.

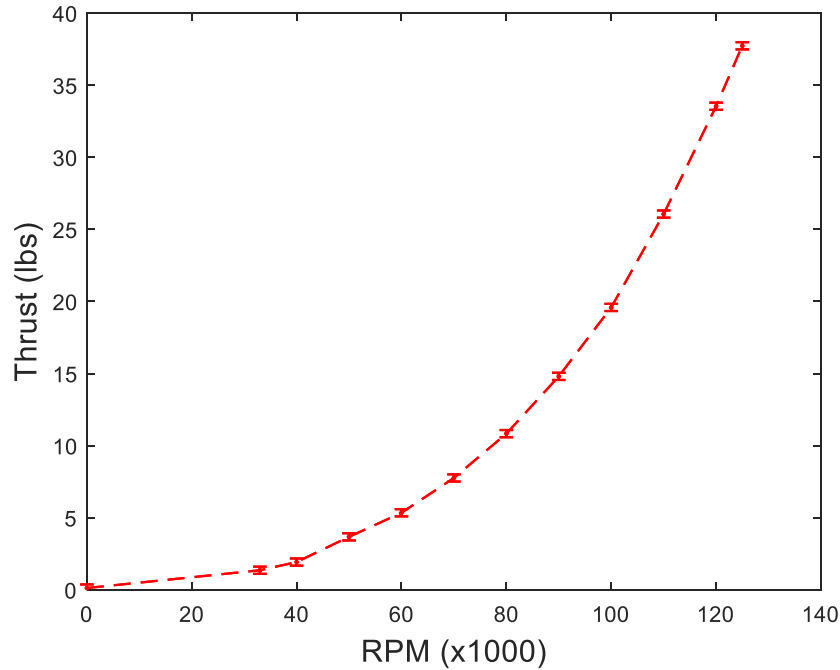


Figure 48: Jet turbine Mach number as a result of increasing RPM

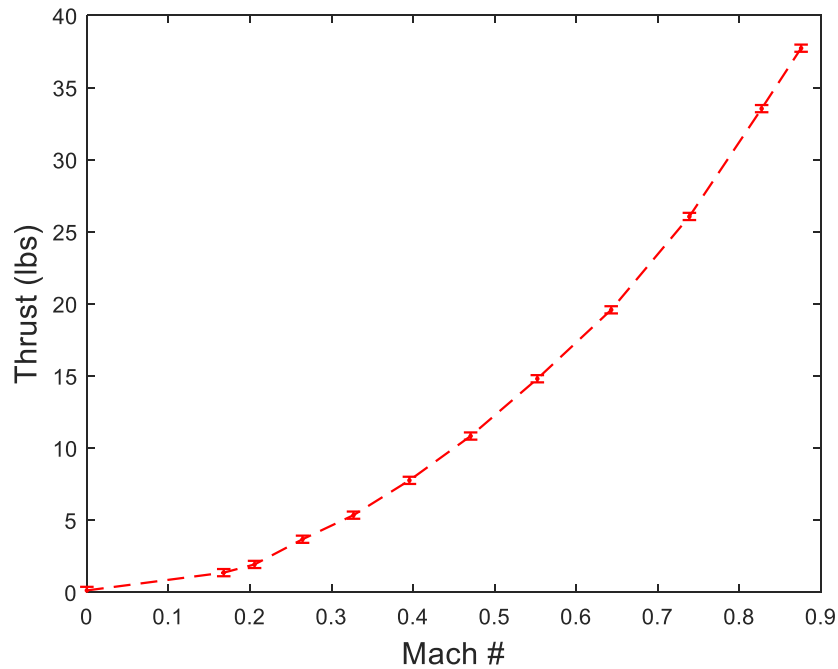


Figure 49: Jet turbine thrust as a function of Mach #

Figure 48 displays the thrust produced by the jet with increasing rpm. The trend follows an exponential as rpm increases. The max thrust at peak rpm was 170N which nearly reaches the manufactures specifications of max thrust equal to 177N at max rpm. The lower thrust may be attributed to friction losses or measurement error. The turbine gets to a compressible state rather quickly after reaching 60,000 rpm and follows an almost linear trend thereon after. Figure 49 shows thrust as a function of Mach number. The thrust also follows an increasing state and looks rather exponential. As the Mach number increases the increase in thrust becomes rampant between the Mach values of 0.4 and 0.88. This is an important relationship as it will be used later to compare to the PETA steady cases.

## CHAPTER IV

### PULSED COLD JET

#### Overview

The following results are from the PETA at both pulsed and steady jet cases with the four different geometrical nozzles and differing Mach number. Some terminology to keep in mind are a free jet is a case in which the set-up does not include the ejector. Therefore, a free steady jet is a jet that does not include an ejector and is free of pulsation. A free pulsed or unsteady jet is a jet which does not include an ejector but is pulsed in which the pulses are described in terms of frequency ( $f$ ).

#### Free Jet Thrust at Different Mach Numbers and Frequencies

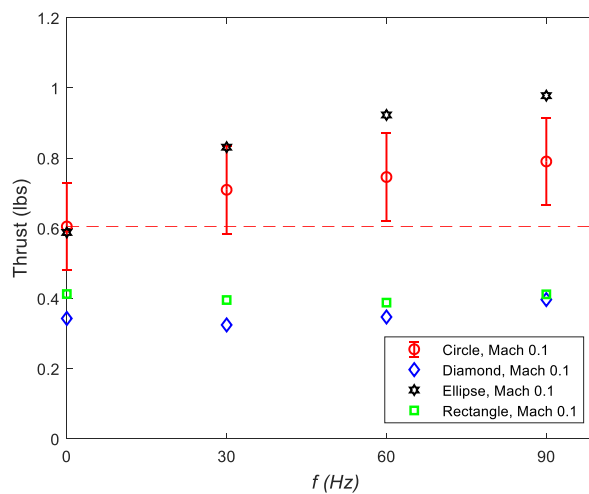


Figure 50: Mach 0.1; thrust against frequency comparing circle, diamond, ellipse and rectangle nozzle geometries for a free jet

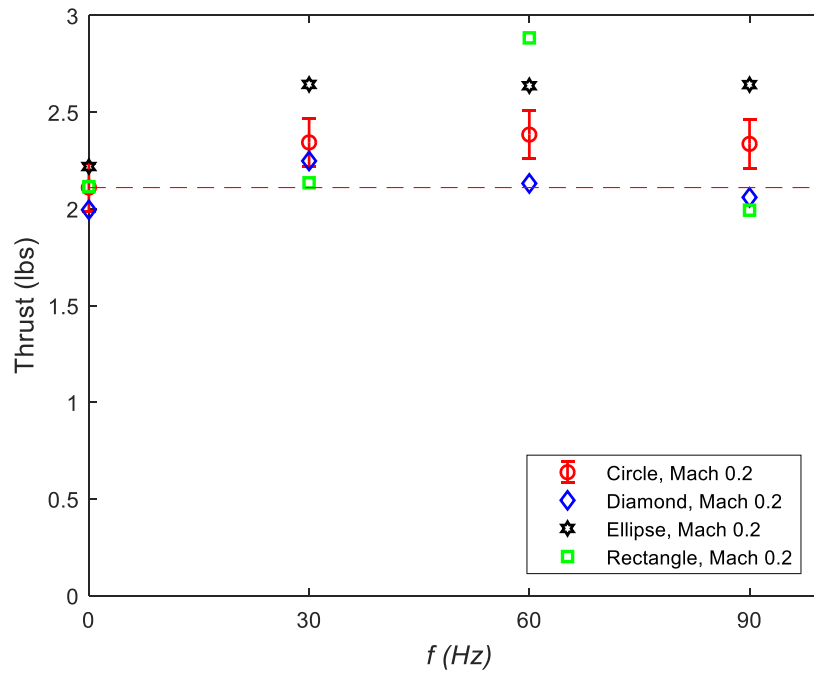


Figure 51: Mach 0.2; thrust against frequency comparing circle, diamond, ellipse and rectangle nozzle geometries for a free jet

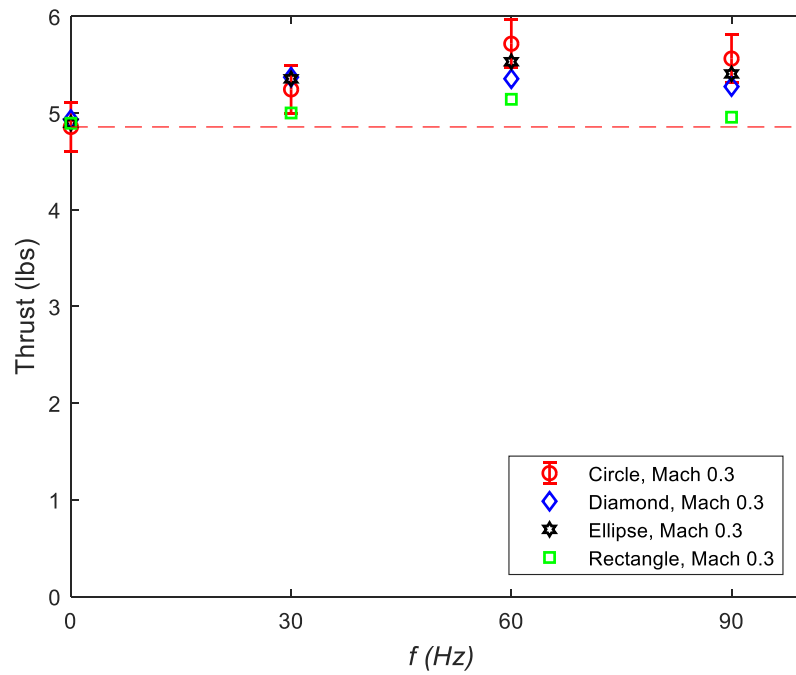


Figure 52: Mach 0.3; thrust against frequency comparing circle, diamond, ellipse and rectangle nozzle geometries for a free jet

Figure 50,51, and 52 show the thrust at steady ( $f = 0$ ) and pulsed states ( $f = 30,60,90$ ) for circular, diamond, ellipse and rectangular nozzle exit geometries for a free jet. The figures convey the increase in thrust when in a pulsed state compared to their steady counterpart as a free jet. Figure 50 shows the biggest net increase for a pulsed ellipse nozzle to occur across all frequencies at Mach 0.1 with the largest increase occurring at 90Hz. The same cannot be said for the diamond nozzle or the rectangular nozzle in where the increase in thrust is below steady conditions. In comparing the circular nozzle to the diamond nozzle, the thrust of the diamond nozzle is well below steady conditions, whereas the circular nozzle presents some values above 0.6 lbs. This tells us that the diamond nozzle produces overall less thrust than the conventional circular nozzle when either in a free steady state or unsteady state. Figure 50 shows the elliptic nozzle performance which has high performers at Mach 0.1 for all frequencies with max thrust occurring at 90Hz. This further affirms the trend that pulsed Mach 0.1 speeds produce more thrust when compared to their free steady cases. The rectangular nozzle struggles to produce thrust for all cases. Though, it can clearly be seen that at Mach 0.2 (Figure 51) at a frequency of 60Hz a substantial increase in thrust is well above any other data point for the rectangle. In Figure 51, the same trend occurs as in Figure 49 in terms that the circle and elliptic nozzles have an overall better performance than the rectangle and diamond. In fact, comparing Figures 50, 51, and 52 results become more clustered as Mach went up.

The circular and elliptic results are similar in the categorize of amount of thrust production by the free jet and the trend in which thrust is increased by pulsing. The elliptic nozzle though, performed better in both these categorize than the circular nozzle. The diamond and square nozzles both under performed in amount of thrust production by the free and pulsating jet. This concludes

that in terms of Mach number for free jets the shapes with sharp corners do not produce as much thrust than those nozzle with smooth features. This may be due to the sharp corners not allowing maximum flow out of the nozzle which can lead to disturbances at the corners creating back flow which takes away from thrust production. Further PIV investigation should be done to determine exactly why geometrical shapes with sharp corners produce overall less thrust in both a free steady jet and a free pulsed jet. It can also be concluded that for smooth edged nozzle with pulsating cases the highest net thrust increases occurred when under Mach 0.1 conditions and in contrast the nozzles with sharp edges seemed to only produce marginal thrust increases from their steady counterparts at all Mach cases, except for the rectangular case at Mach 0.2 and 60hz.

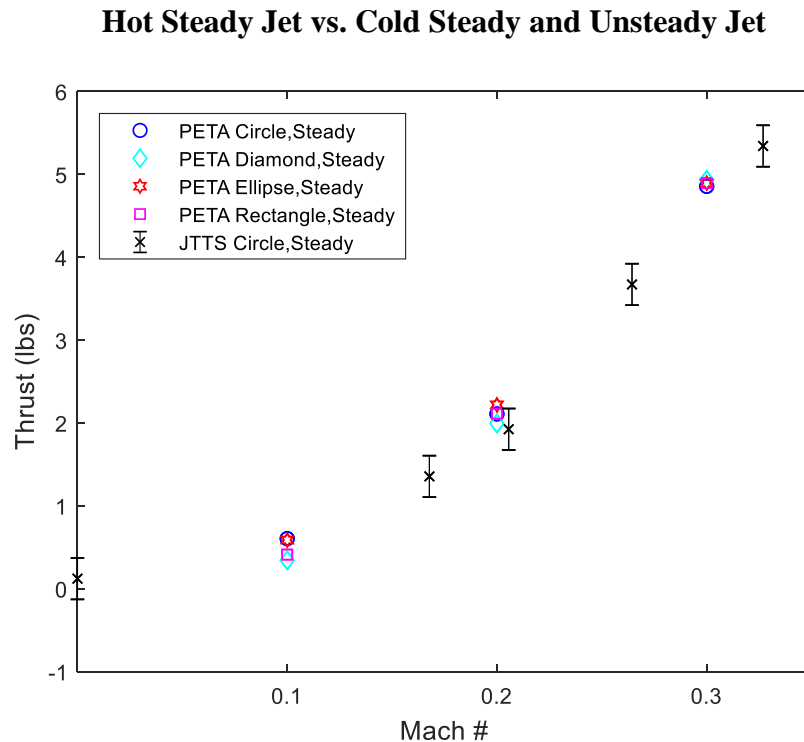


Figure 53: thrust vs Mach # for PETA nozzle shapes at steady conditions and JTTs standard circle nozzle at steady conditions



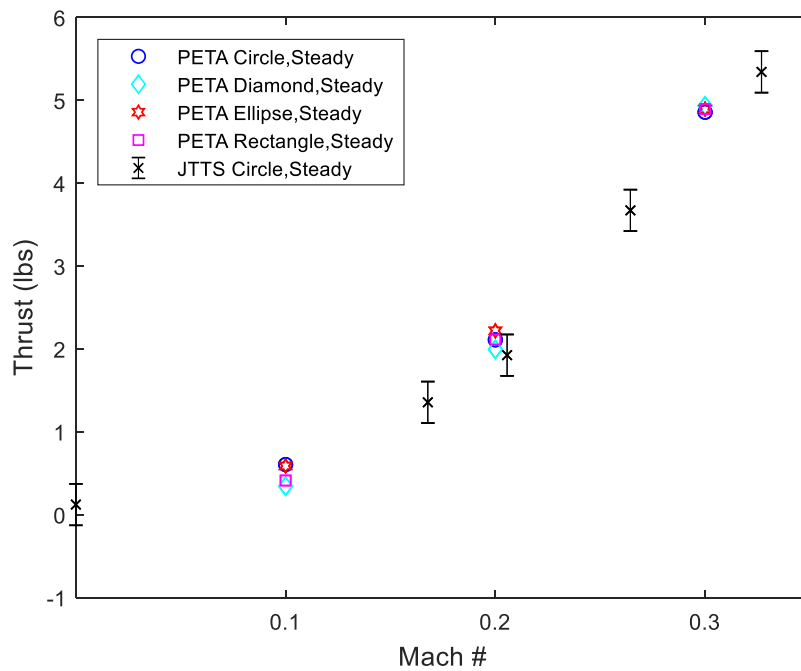


Figure 54; thrust vs Mach # for PETA nozzle shapes at 30Hz and JTTs standard circle nozzle at steady conditions

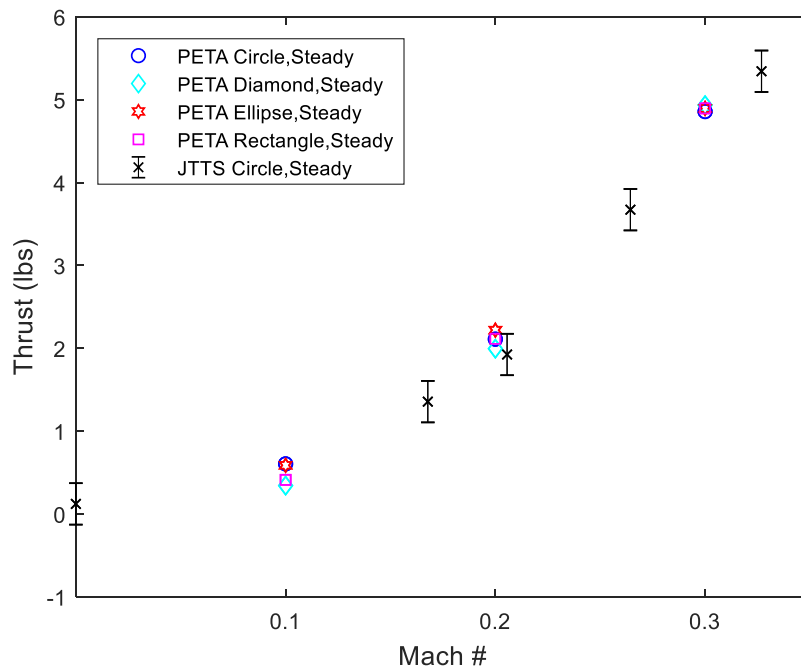


Figure 55; thrust vs Mach # for PETA nozzle shapes at 60Hz and JTTs standard circle nozzle at steady conditions

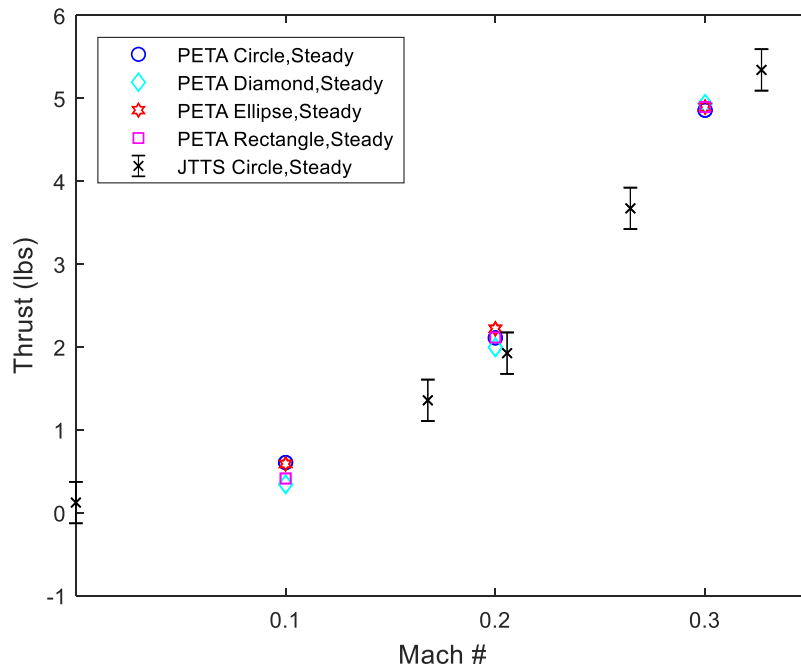


Figure 56: thrust vs Mach # for PETA nozzle shapes at 90Hz and JTTs standard circle nozzle at steady conditions

The above Figures brings together the results from the JTTs and the PETA. As mentioned before what is learned from the PETA will be applied to the JTTs for a more accurate real-world comparison to hot jets used in aeronautic vehicles. Figures 53-56 shows the comparison between PETA and JTTs thrust but at 30hz, 60Hz and 90HZ respectively. Again, similar trends can be seen as the steady jet figure in which the PETA nozzle shapes at increasing Mach number the thrust also increases. When comparing the thrust produced by all cases of the PETA jet to the JTTs jet the PETA seems to produce more thrust at each Mach number. It is also notable to see that when increasing frequency from figure to figure, the thrust produced by the different nozzle seems relatively the same. This could be because there is no ejector to help with the addition entrainment of secondary air, therefore the pulses are only grabbing ambient stationary air which does not further the increase of momentum in the vortex ring.

## Uncertainty Analysis

The operating uncertainty or systematic errors for the JTTS pressure, force and temperature measurements are as follows. The pressure transducer accuracy for combined linearity, hysteresis and repeatability according to the manual is  $\pm 0.25\%$  full scale which corresponds to  $\pm 0.13$ psia. The voltage reading is read through a PCI-6250 which has 2.44mV resolution for -10V to 10V. This corresponds to an uncertainty of 0.048psia and when combining with the pressure transducer corresponds to pressure uncertainty of  $\pm 0.18$ psia. The combined linearity, hysteresis and repeatability accuracy for the load cell is  $\pm 0.5\%$  full scale which corresponds to  $\pm 0.25$ lbs. When combined with the PCI card the uncertainty becomes  $\pm 0.30$ lbs. The J-type thermocouple has an uncertainty of 2.2C or 0.75% depending on which is greater. The maximum temperature for the jet turbine is 700C which gives an uncertainty of 5.25C.

The operating uncertainty systematic errors for the PETA pressure, force and temperature measurements are as follows. The pressure transducer accuracy for combined linearity, hysteresis and repeatability according to the manual is  $\pm 0.25\%$  full scale which corresponds to  $\pm 0.25$ psia. The voltage reading is read through a PCI-6250 which has 2.44mV resolution for -10V to 10V. This corresponds to an uncertainty of 0.048psia and when combining with the pressure transducer corresponds to pressure uncertainty of  $\pm 0.30$ psia. The combined linearity, hysteresis and repeatability accuracy for the load cell is  $\pm 0.5\%$  full scale which corresponds to  $\pm 0.25$ lbs. When combined with the PCI card the uncertainty becomes  $\pm 0.30$ lbs. The K-type thermocouple has an uncertainty of 2.2C or 2% depending on which is greater. The maximum temperature for the cold jet is 550 k which gives an uncertainty of 5.5C.

## JTTS load Cell Uncertainty

Test measurements include systematic and random error components which are a property of the measurements. The uncertainty analysis will draw from the measurements themselves to estimate the range of probable error. For example, the following was done for the load cell of the PETA when a hysteresis analysis was done.

Based on the manufactured specifications the following is done to obtain the systematic error.

$$F.S. = 200lbs \quad (4.1)$$

$$Static\ error = \pm 0.05\% \text{ of } F.S. = 0.10lbs \quad (4.2)$$

$$Nonlinearity = \pm 0.05\% \text{ of } F.S. = 0.10lbs \quad (4.3)$$

$$Creep\ in\ 20\ minutes = \pm 0.025\% \text{ of } F.S. = 0.05lbs \quad (4.4)$$

A hysteresis analysis was done by loading and unloading forces onto the load cell in order to calculate offset. The hysteresis was calculated to be 0.22% of 52 lbs. Therefore,

$$Hysteresis = \pm 0.22\% \text{ of } 52lbs = 0.11lbs \quad (4.5)$$

Squaring the static, nonlinearity, creep, and hysteresis, adding them and square rooting gives us the following.

$$B_x = Systematic\ Error = \sqrt{0.1^2 + 0.1^2 + 0.05^2 + 0.11^2} = 0.19lbs \quad (4.6)$$

The random error is taken from the data collection, First the standard deviation must be taken of the data points, or number of sample “N” from the hysteresis analysis.

$$S_{\bar{x}} = \frac{s}{\sqrt{N}} = \frac{\sqrt{\frac{\sum(x-x_i)^2}{N-1}}}{\sqrt{N}} = 0.11lbs \quad (4.7)$$

The degree of freedom based on the number of samples is  $\mu = N - 1 = 5$ . From this the student t-distribution factor at 95% confidence level can be found which is the following.

$$t_{95} = 2.571 \quad (4.8)$$

Then, taking the standard deviation and dividing by the square root of the number of samples then multiplying by t-distribution factor gives us the following random error.

$$P_x = \text{Random Error} = t_{95} * S_{\bar{x}} = 0.28lbs \quad (4.9)$$

Finally, to find the total uncertainty of the system, the following equation is utilized

$$\text{Total Uncertainty} = \sqrt{B_x^2 + P_x^2} = 0.34lbs \quad (4.10)$$

The above answer of 0.34lbs, means that at each data point there exist an error of 0.34lbs, which can be written as  $\bar{x} \pm 0.34lbs$ . The above analysis was done for all gathered data and is expressed by the utilization of error bars the show the error in the measurement.

## CHAPTER V

### PULSED JET EJECTOR

#### Overview

The following set of figures will take aim at comparing the three different area ratios (AR) of the JTTS ejector described in (Choutapalli I. M., An Experimental Study of a Pulsed Jet Ejector, 2007) at both the steady and unsteady conditions while holding the shape constant. The figures present the data for cases with an ejector for thrust against frequency at differing Mach number and area ratio (AR). The Ejector conjunction point between the super ellipse and the ejector wall was aligned with the exit nozzle trailing edge with a two-inch offset, as the ejector being behind the nozzle. Three different Mach numbers are looked at and are divided into the following three sections.

#### AR 7.6 Unsteady Thrust for Different Mach Numbers and Frequencies

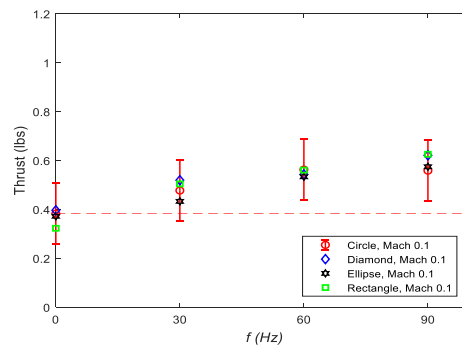


Figure 57: Mach 0.1; thrust against frequency comparing circle, diamond, ellipse and rectangle nozzle geometries for a jet ejector AR 7.

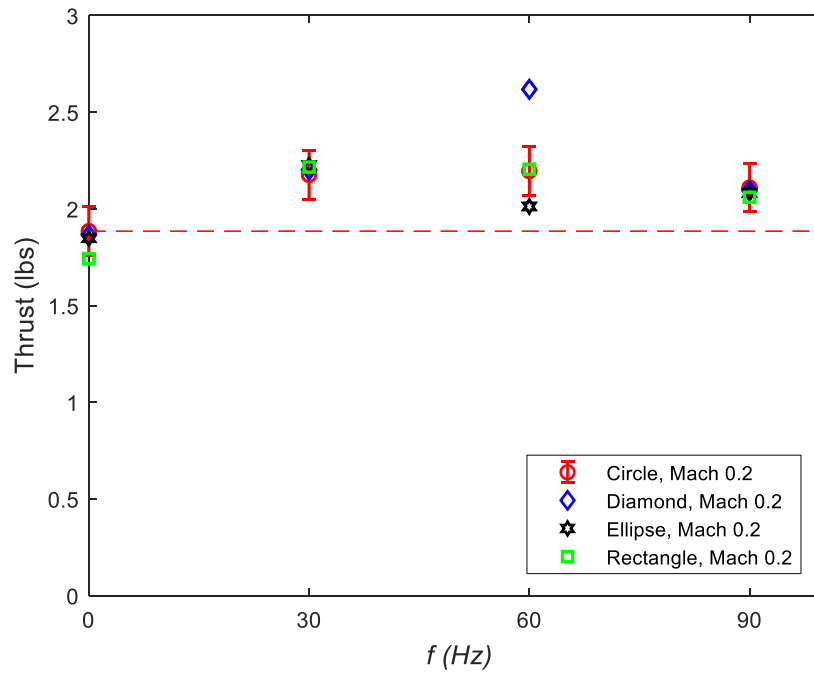


Figure 58: Mach 0.2; thrust against frequency comparing circle, diamond, ellipse and rectangle nozzle geometries for a jet ejector AR 7.6

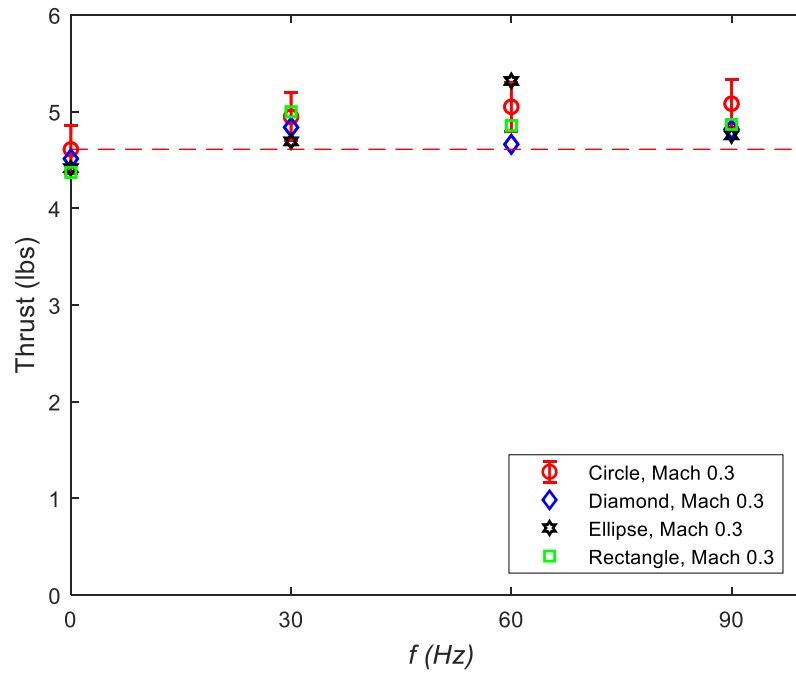


Figure 59: Mach 0.3; thrust against frequency comparing circle, diamond, ellipse and rectangle nozzle geometries for a jet ejector AR 7.6

Figure 57, 58, and 59 all show thrust vs frequency for circular, diamond, elliptic and rectangular nozzles at AR 7.6. Figure 57, 58 and 59 represent Mach 0.1, 0.2, and 0.3 respectively. As can be seen from Figure 57, the overall trend is a monotonic increase in thrust with increasing frequency. At each pulsed case ( $f = 30, 60, 90$ ), the nozzles produced more thrust than their steady counterpart. The highest performers come at 90HZ with the diamond and rectangle nozzles. This may be an indication that at low Mach numbers and high frequencies, nozzles with sharp edges will produce more thrust than those with smooth edges. In Figure 58, the Mach number is increased and the same monotonic trend is no longer seen. Instead, most nozzle shapes performed better when pulsating at 30Hz. This is not true for the diamond nozzle, which performs above all else at 60Hz. The diamond nozzle will not seem to play by the same rules as this study goes on and seems to be more dependent on Mach number than frequency. As will be seen as this study goes on, there seems to exist a relationship between increasing Mach number and decreasing frequency. In Figure 58, the Mach number is increased to its highest value for this study. Again, there is a monotonic increase from 0Hz to 60Hz and then a very slight drop off or no additional thrust is produced for circular and ellipse nozzle. This is not true for the diamond and rectangular nozzle which reach a peak at 30Hz and then steadily decreases for 60Hz. It can be noted that the behaviors of the nozzles seem to be due to their shape at the low AR of 7.6. The circular and elliptic nozzles usually have similar performance, while the diamond and rectangular nozzles have similar performance.



## AR 11 Unsteady Thrust for Different Mach Numbers and Frequencies

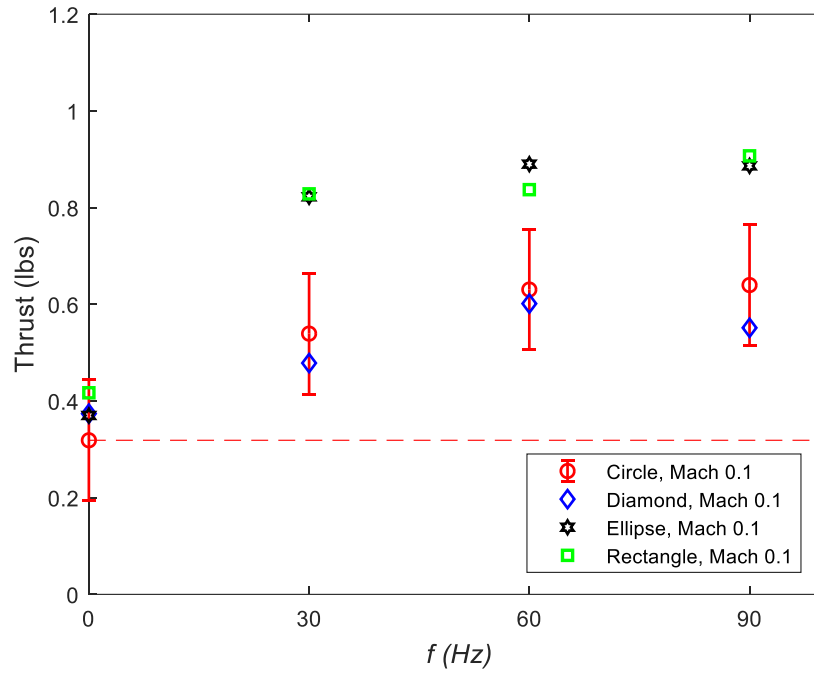


Figure 60: Mach 0.1; thrust against frequency comparing circle, diamond, ellipse and rectangle nozzle geometries for a jet ejector AR 11

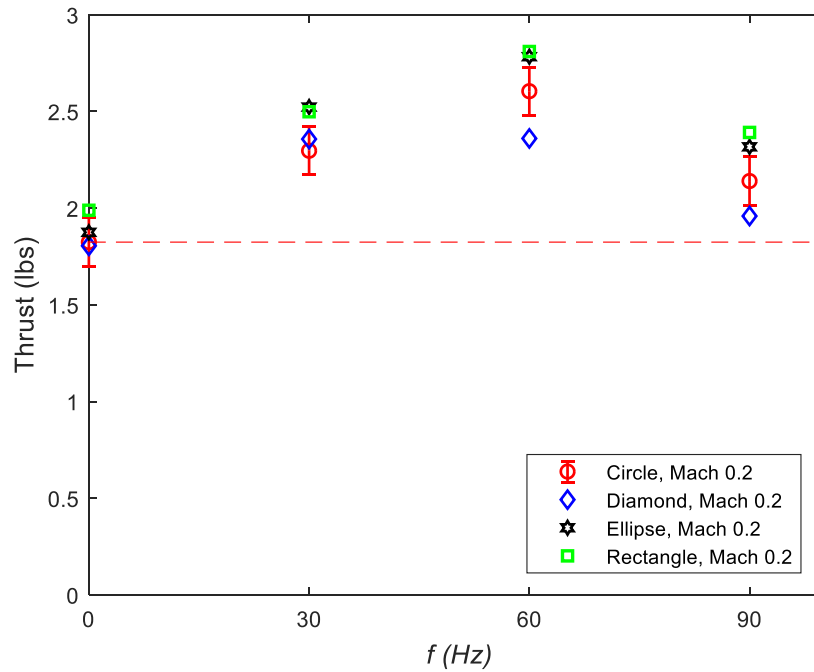


Figure 61: Mach 0.2; thrust against frequency comparing circle, diamond, ellipse and rectangle nozzle geometries for a jet ejector AR 11

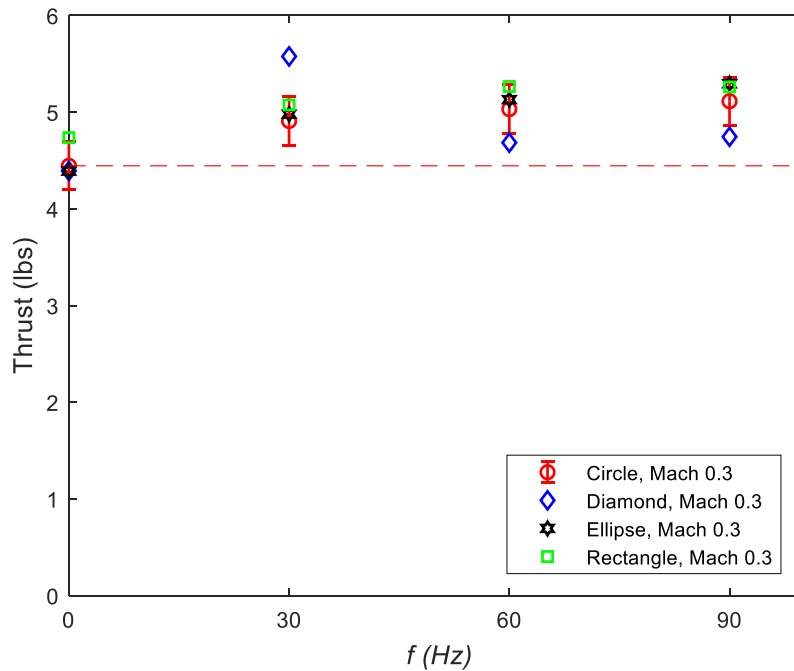


Figure 62: Mach 0.3; thrust against frequency comparing circle, diamond, ellipse and rectangle nozzle geometries for a jet ejector AR 11

Figure 60, 61, and 62 all show thrust vs frequency for circular, diamond, elliptic and rectangular nozzles at AR 11. Figure 60, 61, and 62 represent Mach 0.1, 0.2, and 0.3 respectively. In Figure 60, there is a clear trend and similar performance between the ellipse and rectangle and between the circle and diamond. The ellipse and rectangle clearly perform better under all pulsing frequencies when compared to the circle and diamond. The ellipse and rectangle monotonically increase through all frequencies except for 90Hz, but this fall under the margin of error and can't be said that the trend continues to increase or stay the same. Again, the same increase is seen for the circle and rectangle, with the circle remaining the same and the diamond decreasing in thrust at 90Hz. In Figure 61 the same trend occurs as that of 60, where the ellipse and rectangle are the two higher performers and have similar thrust values versus the circle and diamond nozzles which

were the lower performers. The trend of monotonic increase from 0 to 60Hz is also clearer in this figure when comparing to Figure 60. Figure 61 shows the steep drop off in thrust at 90Hz which was not clear in Figure 62. This tells us that at Mach 0.2, and AR of 11 a frequency of 60Hz is optimum. In Figure 63, the trend continues where the ellipse and the rectangle perform better than the circle and diamond and have a monotonic increase from 0 to 60Hz and at 90Hz seem to provide no addition thrust. The diamond though, does not follow this trend and reaches a maximum thrust at 30Hz then drops at 60Hz and remains the same at 90Hz. The trend for the diamond is still unclear but may be more dependent on Mach number than frequency. When comparing overall the AR of 7.6 to AR of 11, an AR of 11 produced more thrust than any of the cases under an AR of 7.6. This makes sense since the larger area allows for more entrained air to be mixed with the primary stream, therefore producing more thrust.

### AR 12 Unsteady Thrust for Different Mach Numbers and Frequencies

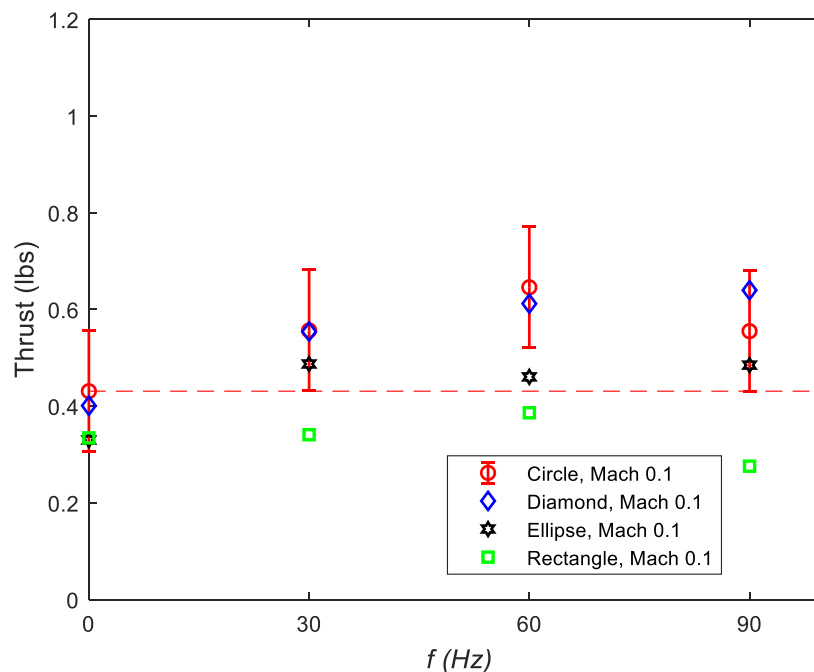


Figure 63: Mach 0.1; thrust against frequency comparing circle, diamond, ellipse and rectangle nozzle geometries for a jet ejector AR 12

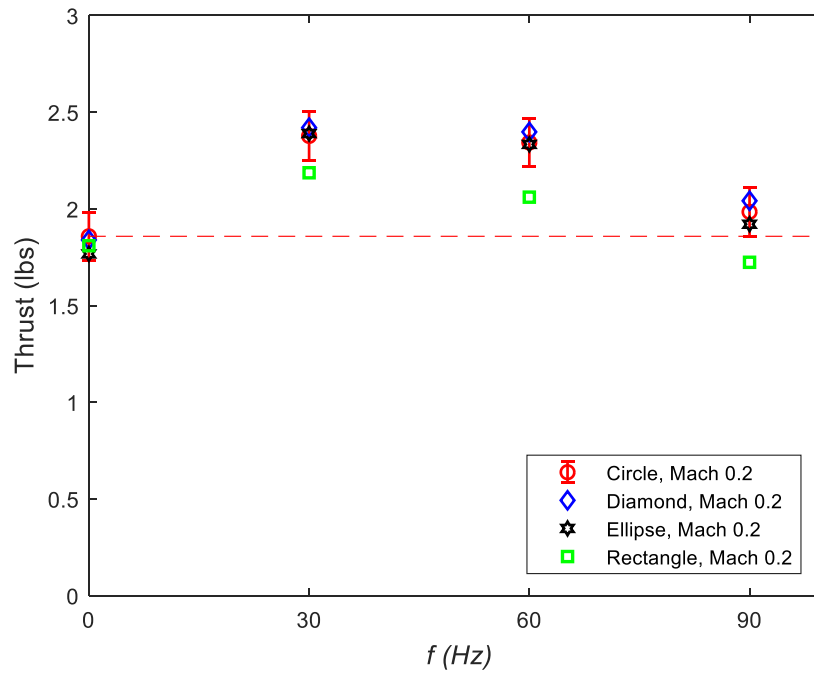


Figure 64: Mach 0.2; thrust against frequency comparing circle, diamond, ellipse and rectangle nozzle geometries for a jet ejector AR 12

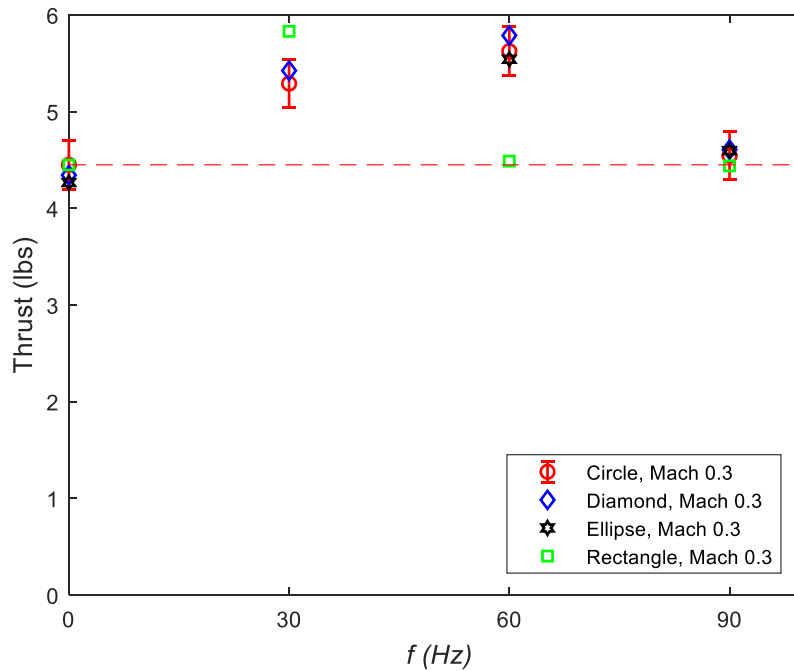


Figure 65: Mach 0.3; thrust against frequency comparing circle, diamond, ellipse and rectangle nozzle geometries for a jet ejector AR 12

Figure 63,64, and 65 all show thrust vs frequency for circular, diamond, elliptic, and rectangular nozzles. Figure 63,64, and 65 represent Mach 0.1, 0.2, and 0.3 respectively. In Figure 63, the circle and diamond nozzles produce the most thrust which is very different from what was seen before. The rectangular nozzle which was a top performer in the previous sections does not even manage to produce more thrust than the steady condition. In Figure 64 the same the rectangle is able to produce more thrust than the steady condition once again with all other nozzles seeming to perform around the same range for each frequency. In Figure 65, the rectangle nozzle is able to only perform better than the steady condition when under 30Hz. The larger AR of 12 seems to be difficult for the rectangular nozzle to entrain air. Further PIV studies should be done in order to find out why this is and why the other three nozzles do not have the same difficulty.

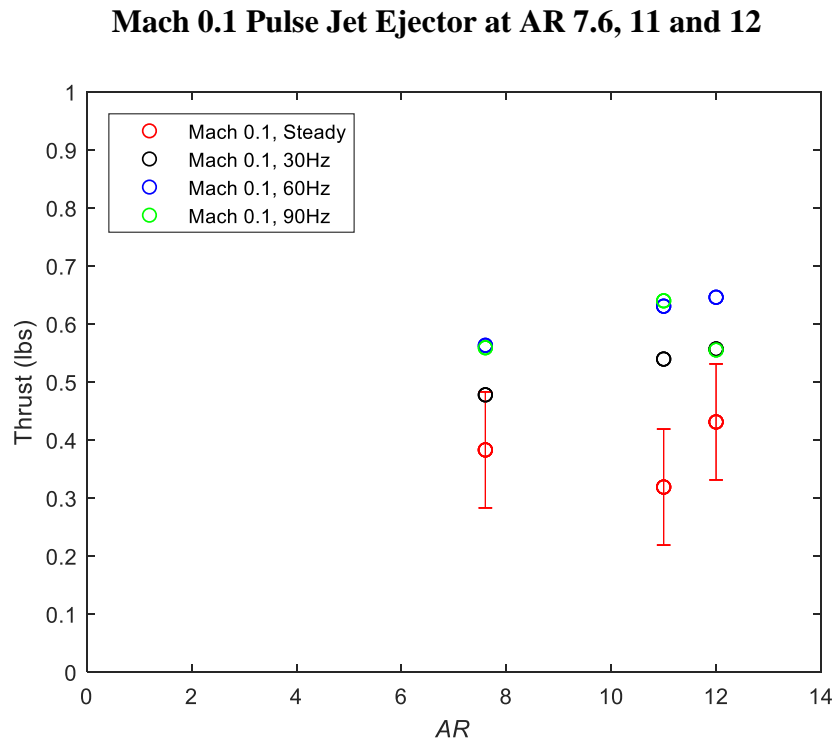


Figure 66: Mach 0.1; Circle nozzle with an ejector; thrust against AR at steady and unsteady cases

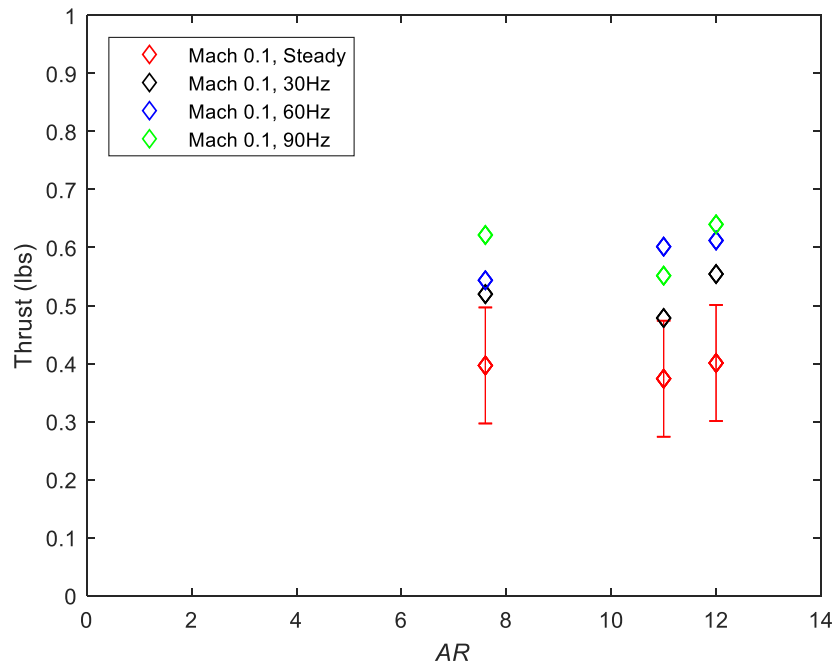


Figure 67: Mach 0.1; Diamond nozzle with an ejector; thrust against AR at steady and unsteady cases

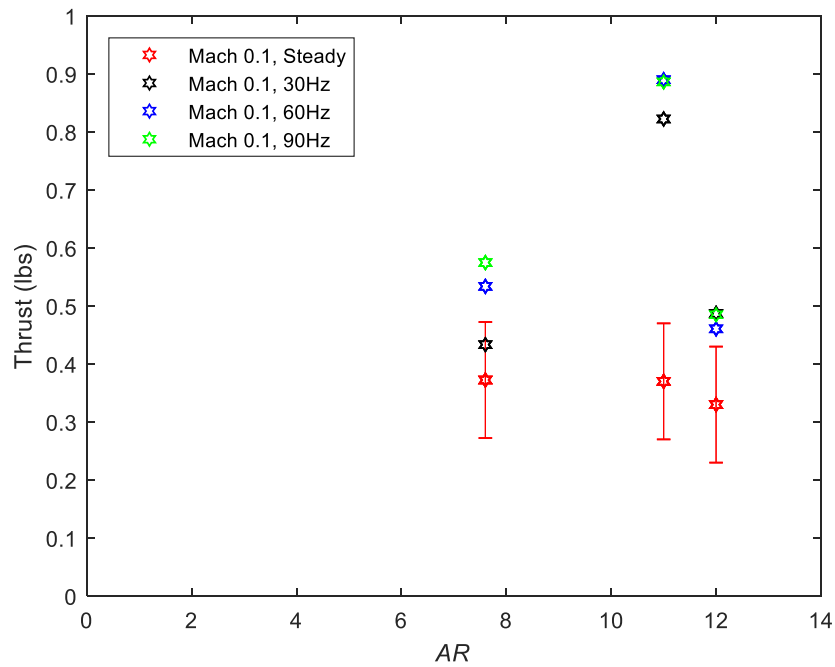


Figure 68: Mach 0.1; Elliptic nozzle with an ejector; thrust against AR at steady and unsteady cases

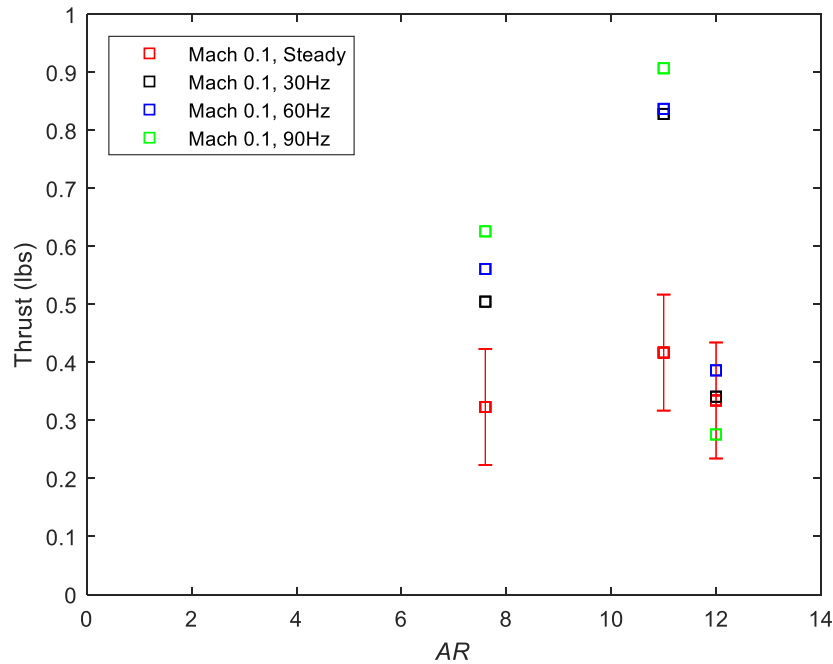


Figure 69: Mach 0.1; Rectangle nozzle with an ejector; thrust against AR at steady and unsteady cases

Figures 66-69 show the thrust vs AR of 7.6, 11 and 12 for the four nozzle configurations respectively for a Mach 0.1. Each figure has data for steady and the three unsteady frequencies and are indicated by colorcode. For all cases it can be seen that the steady jet with an ejector performs lower than the unsteady jets with an ejector. This is to be expected as the addition of the ejector allows the pulsed jet to entrain greater secondary fluid than the steady jet alone. Looking at Figure 66, the unsteady jet at 30Hz performs lower than its 60 and 90Hz counter parts at AR of 7.6 and 11. While at an AR of 12 60Hz pulsing performs the best. In fact, at 60 Hz the thrust is increased at each increasing AR. The general trend for the circular nozzle is that as the AR increases, the thrust also increases with higher pulsing rates generally performing better at each AR.

Figure 67, shows a dip in thrust for all frequencies at an AR of 11 except for the frequency of 65Hz. At 60Hz the diamond nozzle performs similarly to the circular nozzle in which at 60Hz the thrust increases with increasing AR. Again, we also see that overall 30Hz performed lower than 60 and 90Hz for each AR which is similar to the circular nozzle. 90 Hz pulsation performed the best at the AR ratios of 7.6 and 12. When comparing the AR to one another, the AR of 12 at each frequency performed better than the other two AR and their frequencies. It can therefore be said that for a diamond nozzle higher frequencies coupled with the largest AR of 12 produced overall the most thrust.

For Figure 68, there is an obvious increase in thrust at the AR of 11 for all pulsed cases. This is in line from the literature produced by Choutapalli. Again, we see that at higher pulsating rates of 60Hz and 90Hz for the optimum AR of 11 for the ellipse produces the most thrust. This peak at an AR of 11 is also seen in Figure 69 for the rectangular nozzle. The thrust produced by the ellipse and the rectangle are nearly similar in values at an AR of 11 where we also see the trend that at higher pulsing rates produces more thrust at the most optimum AR for the particular nozzle shape.

The question now becomes why is there a general increase in the circular nozzle with each increasing AR while for the diamond nozzle there was a dip for an AR of 11 which is contrary to what was seen for the ellipse and the rectangular nozzle where an AR of 11 saw a significant jump. The answer may be in the way the profile of the jet morphs when exiting the nozzle. As was discussed in Chapter I elliptic and rectangular shaped jets had an axis switching characteristic. The axis switching based on the literature produced better thrust characteristics than the triangle jet which had morphing characteristic rather than axis switching. If this is true for this experiment the



diamond acts as two triangular jets and is not axis switching which is why we see a dip in AR of 11. This also helps us understand why at an AR of 11 for the ellipse and the rectangle there exists a higher thrust which matches the finding of Choutappali. It may also be said that since the circular nozzle does not experience morphing or axis switching due to its symmetry, the thrust for the circular nozzle will change on the basis of AR and frequency alone which could explain the monotonic increase seen in Figure 66. Also the trend for all figures was that at higher frequency of 60 and 90Hz performed better at each AR. This may be due to the coupling of the low Mach of 0.1 with the higher frequency. This will be further discussed in the subsequent sections.

**Mach 0.2 Pulse Jet Ejector at AR 7.6, 11 and 12**

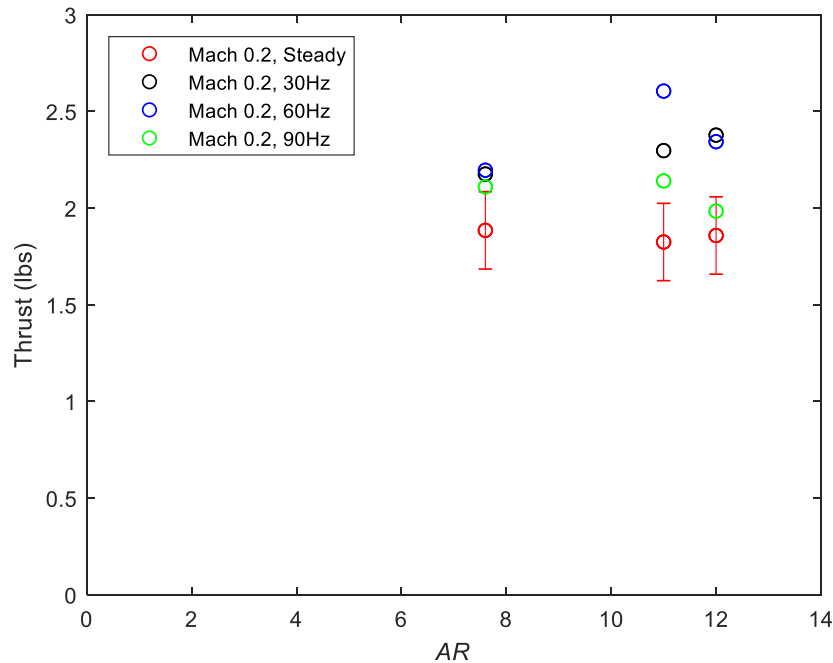


Figure 70: Mach 0.2; Circle nozzle with an ejector; thrust against AR at steady and unsteady cases

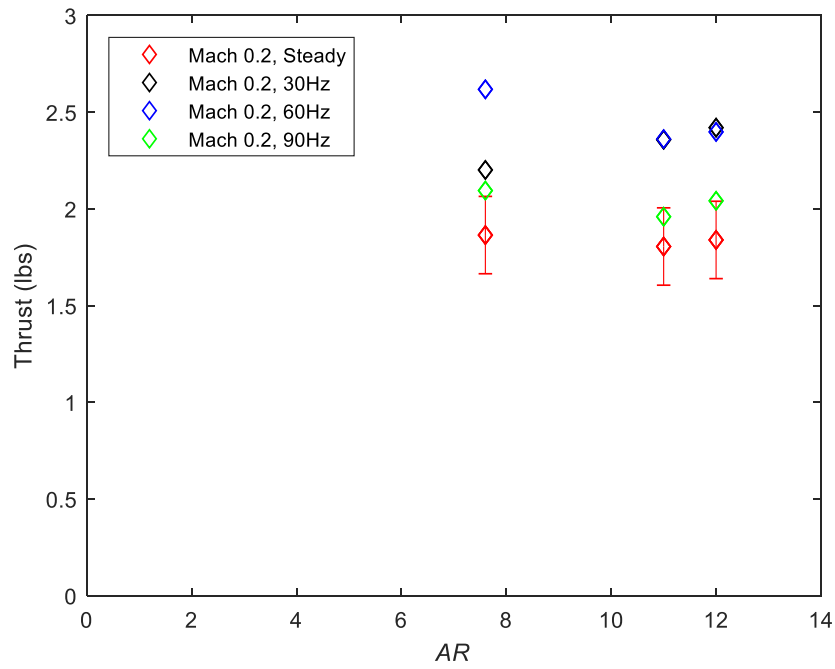


Figure 71: Mach 0.2; Diamond nozzle with an ejector; thrust against AR at steady and unsteady cases

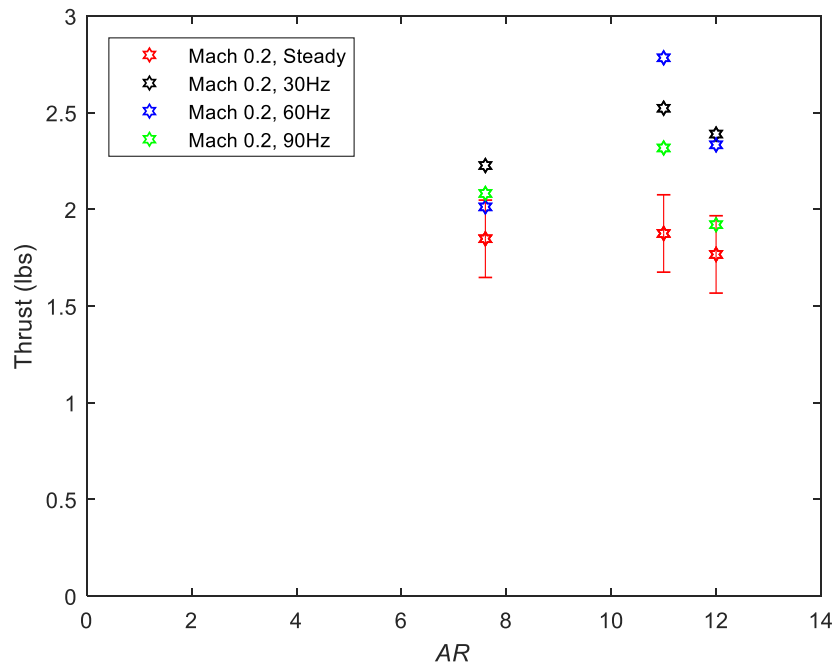


Figure 72: Mach 0.2; Elliptic nozzle with an ejector; thrust against AR at steady and unsteady cases

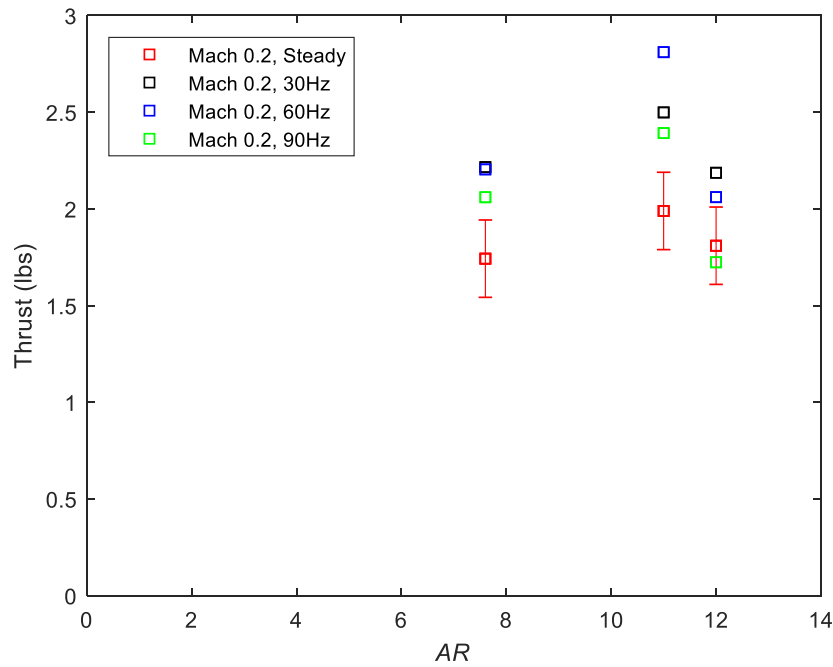


Figure 73: Mach 0.2; Rectangle nozzle with an ejector; thrust against AR at steady and unsteady cases

Figure 70-73 show the thrust vs AR of 7.6, 11 and 12 for the four nozzle configurations respectively for a Mach 0.2. Each figure has data for steady and three unsteady frequencies which are indicated by colorcode. For all cases it can be seen that the steady jet with an ejector performs lower than the unsteady jets with an ejector which we also saw for the Mach 0.1 cases. The circular nozzle data in Figure 70, has an increase of thrust at an AR of 11 for 30 and 60Hz. Over all pulsating at 30 and 60Hz at each AR performed better than pulsing at 90Hz which differs from Mach 0.1. In fact, pulsing at 90Hz did far more poorly than at Mach 0.1. This furthers the idea that there is a relationship between high pulsing and low Mach and vice versa. The general trend for the figure is that better performance occurs at an AR of 11 with mid to low pulsing.

In Figure 71, the trend follows that of Mach 0.1 where there is a dip in performance at an AR of 11. The difference though as was seen in Figure 70, the Mid to low frequencies performed better at each AR and the performance of pulsating at 90Hz significantly drops. Again, there is a relationship that as the Mach number rises there is a relationship that produces higher thrust when pulsating at a lower frequency and vice versa. This trend furthers for the elliptic and rectangular nozzle.

The elliptic nozzle in Figure 72, follows that of its Mach 0.1 counterpart in which at an AR of 11 there is a clear uptick. This can also be seen in Figure 73, where at an AR of 11 the thrust also performs better. The theme until now is that at an AR of 11 performance in thrust when coupled with either 30 or 60Hz produced the most thrust. The optimum AR of 11 seems to coincide with other studies done by *Choutapalli(2007)*. It can also be said that at the mid to low frequency of 30 and 60Hz the ejector of AR 11 performs best. This is not the case for the diamond nozzle where it performed better at AR 7.6 but still keeps the same trend of 30 and 60Hz performing better.

### Mach 0.3 Pulse Jet Ejector at AR 7.6, 11 and 12

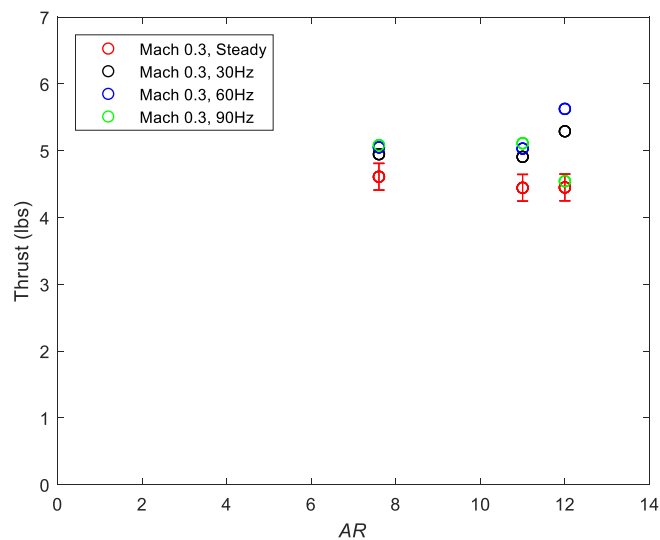


Figure 74: Mach 0.3; Circle nozzle with an ejector; thrust against AR at steady and unsteady cases

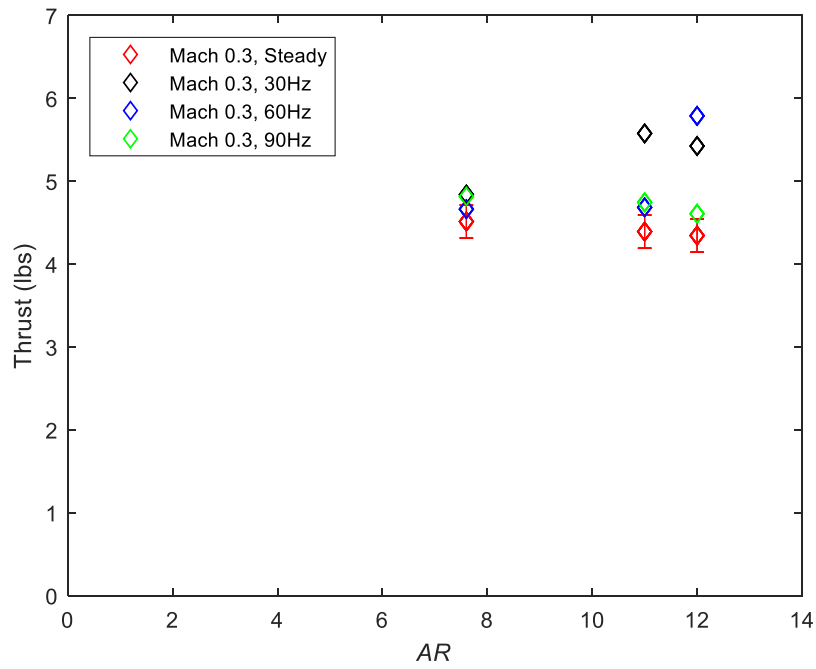


Figure 75; Mach 0.3; Diamond nozzle with an ejector; thrust against AR at steady and unsteady cases

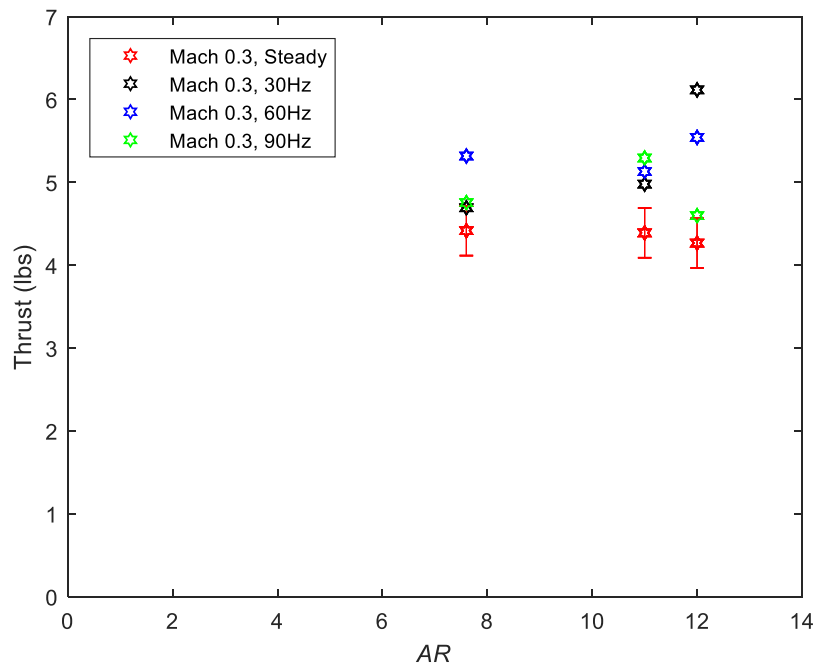


Figure 76; Mach 0.3; Elliptic nozzle with an ejector; thrust against AR at steady and unsteady cases

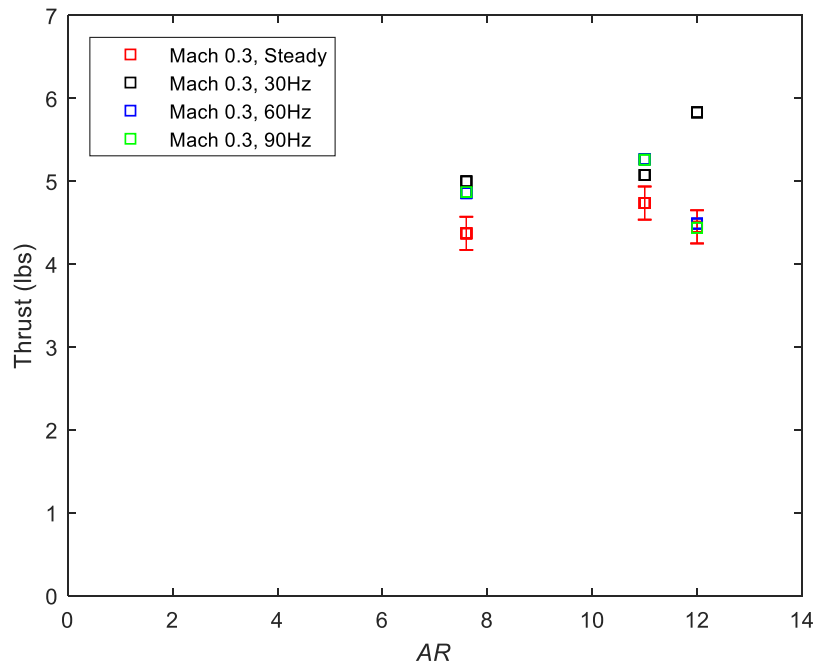


Figure 77: Mach 0.3; Rectangle nozzle with an ejector; thrust against AR at steady and unsteady cases

Figures 74-77 show the thrust vs AR of 7.6, 11 and 12 for the four nozzle configurations respectively for a Mach 0.3. Each figure has data for steady and three unsteady frequencies which are indicated by colorcode. For all cases it can be seen that the steady jet with an ejector performs lower than the unsteady jets with an ejector which we also saw for the Mach 0.1 and Mach 0.2 cases. In Figure 74, the points at an AR of 7.6 seem to become more cluttered together and is nearly identical to that at an AR of 11. The highest performers are at an AR of 12 where again we see that a pulsing frequency of 30 and 60Hz performs better than 90Hz. In fact, pulsing at 90Hz is well in the margin of error for the steady case. The clear difference is that the optimal performance has shifted from an AR of 11 to 12 which is also seen for the diamond nozzle.

In Figure 75, the diamond nozzle follows the same trend found in Figure 74. At an AR of 7.6 all points are within the margin of error of the steady and tells us that with the increased speed the pulsed jet behaves as a steady jet for smaller AR. The trend of lower frequencies of 30 and 60Hz performing better at higher Mach is again reaffirmed when looking at the AR of 12.

For Figure 76 and 77 we continue to see the same trends of pulsing at an AR or 7.6 almost acting as a steady jet. In Figure 76, the best performers are again at an AR of 12 and pulsing frequencies of 30Hz and 60Hz with 30Hz being well above the 60Hz pulsing. The rectangular nozzle differs from the elliptic nozzle in that at an AR of 12 all frequencies act as a steady jets except for at 30Hz. This tells us that at the higher speed the rectangle is no longer entraining secondary fluid which is most likely due to the geometry not being able to entrain secondary air to create more momentum in the vortex rings at such a high speed unless the pulsing is significantly reduced.

As was stated in this section, with the higher Mach number, there was a shift from the optimum AR being 11 for most cases to being 12 for all cases. This is because at higher speeds and lower AR, the secondary fluid is no longer able to mix properly with the primary fluid and smaller amounts get through the ejector due to the larger jet stream. Instead the secondary fluid that is able to entrain into the ejector is now just pushed alongside the primary jet and acts as almost a steady jet.

### **1-D Theoretical Analysis for steady jet ejector**

The following control volume analysis was done to show the difference in entrainment of secondary stream between a circular nozzle and a rectangular nozzle. The following schematic

establishes the control volume. The continuity and momentum equations along with the Bernoulli equation to define the secondary jet entrainment were utilized.

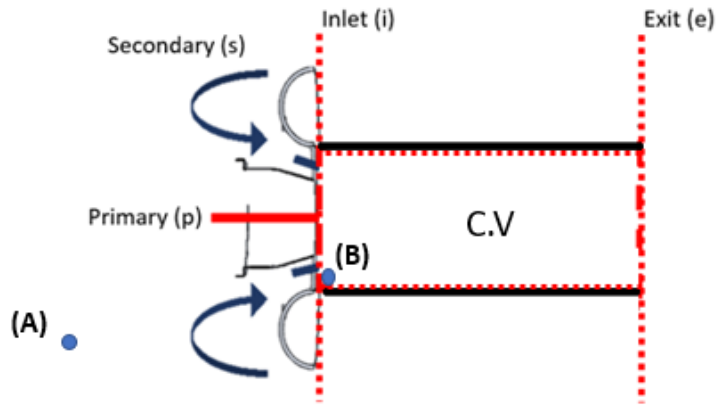


Figure 78: Ejector schematic establishing C.V.

### Continuity

$$A_e V_e = V_p A_p + V_s A_s \quad (5.1)$$

Dividing by exit area and squaring both sides produces the following

$$V_e^2 = V_p^2 \left( \frac{A_p}{A_e} \right)^2 + V_s^2 \left( \frac{A_s}{A_e} \right)^2 + 2V_p V_s \frac{A_p A_s}{A_e^2} \quad (5.2)$$

$$V_e^2 A_e = V_p^2 \frac{A_p^2}{A_e} + V_s^2 \frac{A_s^2}{A_e} + 2V_p V_s \frac{A_p A_s}{A_e}$$

The above continuity equation will later be used in conjunction with the momentum equation

### Momentum



$$(P_B - P_A)A_e = \rho V_e^2 A_e - \rho V_p^2 A_p - \rho V_s^2 A_s + \int \frac{\partial V}{\partial t} \rho d(vol) \quad (5.3)$$

Due to body forces being disregarded the following momentum equation is produced

$$(P_B - P_A)A_e = \rho V_e^2 A_e - \rho V_p^2 A_p - \rho V_s^2 A_s \quad (5.4)$$

### Bernoulli

$$\frac{P_A}{\rho} - \frac{P_B}{\rho} = \int_A^B \left[ \frac{\partial V}{\partial t} ds \right] + \frac{V_s^2}{2} \quad (5.6)$$

Since the jet is a function of time the middle term is cancelled and results in

$$\frac{P_A - P_B}{\rho} = \frac{V_s^2}{2} \quad (5.7)$$

Applying the above bernoulli equation to the momentum equation yields

$$V_e^2 A_e = V_p^2 A_p + V_s^2 A_s - \frac{V_s^2}{2} A_e \quad (5.8)$$

Equating the above expression to the continuity equation yields

$$V_p^2 \frac{A_p^2}{A_e} + V_s^2 \frac{A_s^2}{A_e} + 2V_p V_s \frac{A_p A_s}{A_e} = V_p^2 A_p + V_s^2 A_s + V_s^2 A_s - \frac{V_s^2}{2} A_e \quad (5.9)$$

Using the equation for mass flow rate  $m = \rho VA$  and defining the area ratio as  $\alpha = \frac{A_s}{A_p}$  the above

equation was rearranged and simplified to produce the following.

$$\frac{m_s^2}{m_p^2} + \frac{1}{\alpha^2} \frac{m_s^2}{m_p^2} + 4 \frac{m_s}{m_p} - 2\alpha = 0 \quad (5.10)$$

The above expression defines the ejector pumping of the combined ejector nozzle augmentor. The pumping is due to the secondary mass flow rate being entrained by the primary mass flow rate which can be seen in the above equation. It can also be seen that ejector pumping is also a factor of area ratio.

The ejector pumping equation was plotted to show the effects of area ratio on the pumping ratio. It is known from theoretical analysis that a rectangular nozzle entrains about 25% more secondary fluid than a circular nozzle. Figure 79 compares a circular nozzle with a rectangular nozzle for pumping ratio at an increasing area ratio where a 25% increase in pumping for the rectangular nozzle was taken into consideration. Figure 79 shows that the mass flow rate ratios for both circle and rectangular nozzles increase when area ratio increases. It also clearly shows that the mass flow rate ratio of the rectangular nozzle performs better than the circular nozzle at every instance. These results are consistent with the findings in the experimental data. The rectangular nozzle in the experimental data consistently produced more thrust than that of the circular data due to the additional entrainment of secondary stream.

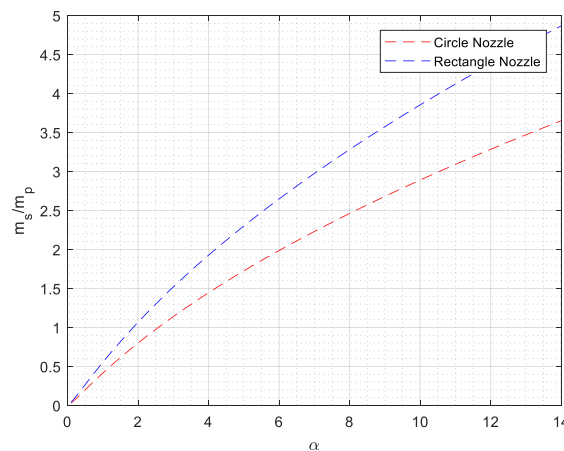


Figure 79: Ejector pumping as a function of area ratio

## CHAPTER VI

### CONCLUSIONS AND FUTURE WORK

#### **Conclusions**

In the study a JTTS and a PETA were used for thrusting experimentation. The JTTS results serve as a baseline and characterize the thrust performance and jet stream of the jet turbine. The jet turbine proved to produced thrust values specified by the manufacturer and nearly reached sonic conditions at maximum RPM. The PETA experimentation was much more involved and tested the effects of four asymmetric nozzle shapes and their effects under free steady and free unsteady conditions as well as the thrust performance when an ejector was added to the system under steady and unsteady conditions. The JTTS free steady thrust and PETA free steady and unsteady thrust were compared and found that the PETA was comparable to the JTTS and even exceeded performance of the JTTS at low Mach numbers. It was also found that as Mach number increased for the pulsed cases, the thrust produced by the differing jet streams became more and more alike. Experiments were then done for the Pulse Jet Ejector cases and varying Mach number. The circular, diamond, ellipse, and rectangular nozzle all performed better when under a pulsed ejector case in comparison to a steady ejector case due to the vortex ring entraining additional secondary air. It was also found that potential axis switching from the elliptic and rectangular nozzles could be due to their generally higher thrust production. It was also found that as Mach number increases

and the frequency increased, the produced thrust was not high when coupled with a lower pulsating frequency. This is because at high Mach number and high frequency the vortex ring is no longer as organized. The coupling of low Mach number and mid to low frequency seems to be the ideal case for creating compact vortex rings and subsequent higher thrust. It was also found that for most Mach numbers and their associated nozzle geometries an AR of 11 performed the best. This is consistent with the finding of Choutapalli(2007). Finally, it was observed that at a high Mach number the AR needs to be larger due to the jet stream being larger and not allowing the secondary stream to be entrained and properly mixed in the ejector.

### **Future Work**

For future studies an ejector is designed based on the literature given in Chapter 1. The design of the ejector was created using SolidWORKS 2019 and is shown in Figures 80 and 81. Figure 79 shows an exploded view of the ejector prototype where three main components make up the prototype; super elliptical inlet, coupling ring, and divergent shroud. The super elliptical is based on the super elliptic which exists in the ejector of the PETA.

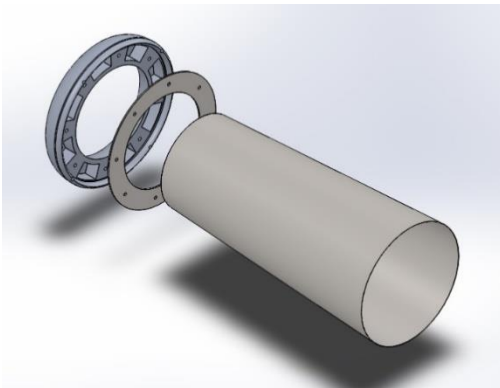


*Figure 80: Exploded view of ejector prototype*

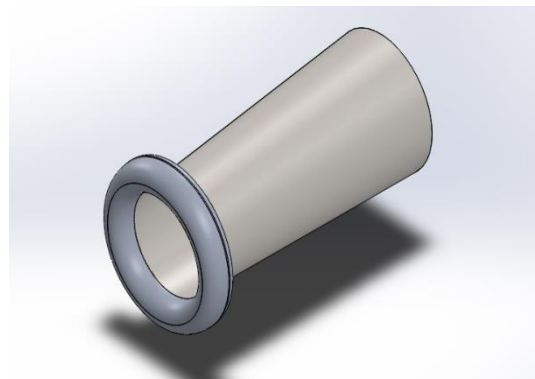


*Figure 81: Ejector prototype CAD model*

## REFERENCES

- Allgood, D., Ephraim, G., Hoke, J., & Bradley, R. (2008). Performance Studies of Pulse Detonation Engine Ejectors. *Journal of Propulsion and Power*, 24.
- Bevilaqua, P. M. (1987). *Advances in ejector thrust augmentation*. Lockheed Aeronautical Systems CO., United States: SAE Technical Papers.
- Choutapalli, I. M. (2007). *An Experimental Study of a Pulsed Jet Ejector*. Florida State University, College of Engineering. Tallahassee: Florida State University Libraries.
- Choutapalli, I. M. (2010). Effect of Mach number on the thrust augmentation and flow field of pulsed jets with and without an ejector. *International Powered Lift Conference*, (pp. 171-185).
- Choutapalli, I. M., Krothapalli, A., & Alkisar, M. B. (2012). Pulsed-Jet Ejector Thrust Augmentor Characteristics. *Journal of Propulsion and Power*, 20(2).
- Figliola, R. S., & Beasley, D. E. (2001). *Theory and Design for Mechanical Measurements*. 5th edition: John Wiley & Sons, Inc.
- Greitzer, E., Paterson, R., & Tan, C. (1985). Approximate substitution principle for viscous heat conduction flows. *Proc. of Royal Society*, 163-193.
- Heiser, W. (2010). Ejector Thrust Augmentation. *Journal of Propulsion and Power*, 26(6), 1325-1330.
- Heiser, W. H. (1967). Thrust Augmentation. *Journal of Engineering Power*, 75-81.
- Hoke, J., A.G., N., & L.P., G. (2009). *Schlieren Imaging of a Single-Ejector, Multi-Tube Pulsed Detonation Engine*. Wright-Patterson Air Force Base, Ohio: American Institute of Aeronautics and Astronautics.
- MI, J., Nathan, G., & Luxton, R. (2000). *Centerline mixing characteristics of jets from nine differently shaped nozzles*. Springer, Experiments in Fluids.
- Miller, R., Madnia, C., & P., G. (1996). *Numerical Simulation of Non-circular Jets*. Buffalo, New York: Elsevier Science.
- National Instruments. (2016). DAQ M Series User Manual.

- Okpara, E. C., & Agarwal, R. K. (2008). Numerical Simulation of Steady and Pulsed Flow through Thrust Augmenting Ejectors. *46th AIAA Aerospace Science Meeting and Exhibit*. Reno, Nevada.
- Paxson, D. E., Wilson, J., & Dougherty, K. T. (2002). Unsteady Ejector Performance: An Experimental Investigation Using a Pulsejet Driver. *38th AIAA/ASME/SAE/ASEE Joint Propulsion Meeting and Exhibit*. Indianapolis, IN.
- Porter, J. L., & Squyers, R. (1981). An Overview of Ejector Theory. *AIAA Aircraft Systems and Technology Conference*. Dayton, Ohio.
- Presz, W. J., & Greitzer, E. M. (1988). A Useful Similarity Principle for Jet Engine Exhaust System Performance. *AIAA/ASME/SAE/ASEE 24th Joint Propulsion Conference*. Boston, Massachusetts.
- Presz, W. J., Reynolds, G., & Hunter, C. (2002). Thrust Augmentation with Mixer-Ejector Systems. *40th AIAA Aerospace Science Meeting & Exhibit*. Reno, NV.
- Quinn, B. (1973). Compact Ejector Thrust Augmentation. *Journal of Aircraft*, 10(8), 481-486.
- R.M., L. (1963). *Interim Summary Report on Investigation of the Process of Energy Transfer from an Intermittent Jet to Secondary Fluid in an Ejector-type Thrust Augmenter*. Hiller Aircraft Corp. Report ARD-305.

## BIOGRAPHICAL SKETCH

Orlando Rodriguez was born and on December 14, 1993 in McAllen, Texas. Mr. Rodriguez grew up in the McAllen where he then went to the University of Texas – Rio Grande Valley where he earned a Bachelor of Science in Mechanical Engineering in May of 2017. Mr. Rodriguez went on to pursue his masters after graduation. He earned his Master of Science degree in Mechanical Engineering in August of 2019. Mr. Rodriguez will continue his engineering career as an engineer for the Boeing Company.

Permanent Address: 4001 Hickory Avenue, McAllen, Texas, 78501

Permanent Email: orlando.rodriguez2109@gmail.com